Dynamic Regulation of Innate Lymphoid Cell Development During Ontogeny

Tao Wu[1,3,7], Sijie Chen[2,7], Jie Ma[4,7], Xinyi Zhu[1,3,7], Maocai Luo[1], Yuanhao Wang[1], Yujie Tian[1], Qingqing Sun[1], Xiaohuan Guo[1], Jianhong Zhang[1], Xuegong Zhang[2,5,*], Yunping Zhu[4,*], Li Wu[1,3,6,8*]

[1]School of Medicine, Institute for Immunology, Tsinghua University, Beijing, 100084, China.

[2]MOE Key Lab of Bioinformatics/Bioinformatics Division, BNRIST and Department of Automation, Tsinghua University, Beijing, 100084, China.

[3]Tsinghua-Peking Center for Life Science, Beijing, China.

[4]State Key Laboratory of Proteomics, Beijing Proteome Research Center, National Center for Protein Sciences (Beijing), Beijing Institute of Life Omics, Beijing 102206, China.

[5]School of Life Sciences, Tsinghua University, Beijing, 100084, China.

[6]Beijing Key Laboratory for Immunological Research on Chronic Diseases, Beijing 100084, China.

[7]These authors contributed equally

[8]Lead Contact

*Correspondence: zhuyunping@gmail.com (Y.Z.), zhangxg@tsinghua.edu.cn (X.Z.), wuli@tsinghua.edu.cn (L.W.)

Graphical abstract

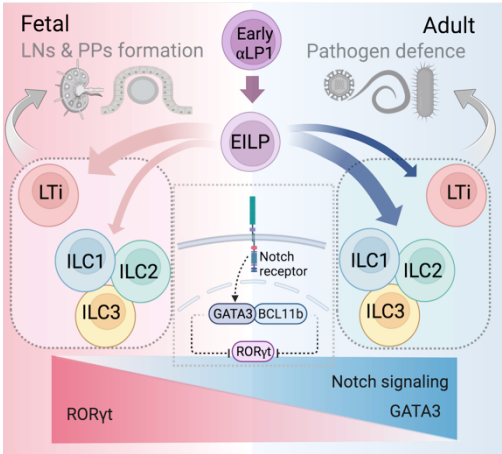

Highlight

- The ratio of LTi cells to non-LTi ILCs decreases from fetal to adult stage
- Modified fate determination of ILC progenitors contributes to this decrease of LTi cell ratio during ontogeny
- A conserved trajectory exists from early αLPs to Innate Lymphoid Cell

Precursors (ILCPs) during both fetal and adult ILC development

- Enhanced activity of Notch-GATA3 signaling in ILC precursors accounts for the transition of their differentiation from LTi cells in the fetal to non-LTi ILCs in adults.

SUMMARY

Innate lymphoid cells (ILCs) are crucial for maintaining tissue homeostasis. The dynamic composition of ILC subsets during ontogeny has been observed for over a decade, yet the underlying mechanisms remain incompletely understood. Here, we combined differentiation assay and scRNA-seq analysis to compare the fetal and adult ILC development, and assessed their contribution to the dynamic change of ILC subsets. We revealed the preference for LTi cell differentiation in fetal hematopoietic progenitors, contrasted with a non-LTi differentiation bias in adult stages. Our analyses elucidated that the two stages shared a conserved differentiation trajectory and regulatory programs but used different controlling logic. Through computational prediction and dose-response experiments, we proposed a model where a transition from fetal RORγt-dominant states to adult Notch-GATA3-dominant states orchestrates these changes. This study suggests that ILC development can be modulated to accommodate the varying demands for specific ILC subsets within the body at different developmental stages.

INTRODUCTION

Innate lymphoid cells (ILCs), the innate counterparts of T cells (Vivier et al., 2018; Walker et al., 2013), encompass a diverse array of cell types including NK cells, ILC1s, ILC2s, ILC3s, and lymphoid tissue inducer (LTi) cells (Bal et al., 2020; Vivier et al., 2018). The ILC3s and LTi cells are also refered as RORγt$^+$ ILCs. Originating predominantly from common lymphoid progenitors (CLPs), ILCs undergo differentiation through a series of progenitor stages, including early innate lymphoid progenitors (EILPs) (Yang et al., 2015), common helper innate lymphoid progenitors (CHILPs) (Klose et al., 2014), and innate lymphoid precursors (ILCPs) (Constantinides et al., 2014), all are included in $\alpha_4\beta_7^+$ lymphoid progenitors (αLPs). Different ILC subset pariticipate

in different facets of immune responses: NK cells and ILC1s produce IFN-γ to defend against viruses and intracellular bacteria; ILC2s secrete IL-4/5/13, playing a role in defense against parasitic infections and in promoting allergies; ILC3s and LTi cells produce IL-17A/22 for defense against extracellular bacteria, crucial for maintaining local tissue homeostasis, particularly at mucosal sites (Bal et al., 2020; Vivier et al., 2018). LTi cells are also pivotal in forming secondary lymphoid tissues, such as lymph nodes and Peyer's patches, primarily during the embryonic stage (Eberl et al., 2004; Onder and Ludewig, 2018).

Previous studies have demonstrated that the composition of ILC subsets exhibits dynamic shifts in various organs throughout murine development, reflecting adaptations to evolving physiological demands essential for maintaining homeostasis. LTi cells, predominant in the neonatal thymus, are scarcely present in adults, while ILC2s emerge as the dominant subset in the adult thymus (Jones et al., 2018). This trend of LTi cell proportions is also observed in the mouse small intestine (Sawa et al., 2010) and human tonsils and is associated with an increase in ILC3s (Hoorweg et al., 2012).

A consistent pattern in the shift of ILC subsets was suggested in the organs mentioned above. Nonetheless, the dynamic distribution of ILC subsets across various tissues remains to be systematically explored and summarized. Furthermore, while microenvironmental alterations are recognized as a primary external driver of ILC subset variations, the extent to which cell-intrinsic differentiation potential contributes to these variations remains ambiguous. Given the significant differences between hematopoietic progenitors at fetal and adult stages, these intrinsic cellular factors are likely to play a crucial role. Another significant challenge is the paucity of comprehensive profiling of ILC progenitors during fetal development, as current identification methods are primarily based on adult bone marrow studies.

In this study, we observed an elevated proportion of lymphoid tissue inducer (LTi) cells in various organs, including lymphoid (spleen) and non-lymphoid organs (small intestine, colon, lung, and liver) during fetal and

newborn stages. Notably, the LTi cell ratio demonstrated a gradual decrease, concomitant with an increase in non-LTi innate lymphoid cells (ILCs) in adulthood. Concurrently, we found ILC progenitors from fetal liver exhibited a preferential differentiation towards LTi cells, whereas those derived from adult bone marrow showed an inclination to differentiate into non-LTi ILCs. This pronounced shift in differentiation preference was observed to occur within just one week post-birth. To elucidate the underlying mechanisms, we utilized single-cell RNA sequencing (scRNA-seq) to reconstruct the ILC developmental landscapes, identifying a conserved developmental trajectory from early αLPs to ILC precursors (ILCPs) in both fetal liver and adult bone marrow. Comparative analysis revealed enhanced Notch signaling and GATA3 expression, alongside reduced RORγt levels in adult progenitors compared to their fetal counterparts. Subsequent systematic dose-response experiments corroborated a “seesaw” model, articulating an interplay between Notch-GATA3 signaling and RORγt during murine ontogeny, which governs the dynamic shifts in ILC subsets. This model elucidates the predisposition of fetal ILC progenitors towards LTi cell differentiation, in contrast to the preference exhibited by adult progenitors.

RESULTS

Ratio of LTi cells to non-LTi ILCs decreases during ontogeny

To investigate the ontogenic distribution of ILCs, we systematically analyzed major ILC subsets in lymphoid (spleen) and non-lymphoid organs (small intestine, colon, lung, and liver) across various developmental stages in mice. The dynamic composition of ILC subsets in these organs reached a stable state within two weeks after birth (Figure 1 and Figure S1). Moreover, three categories of the ILC composition could be grouped based on their dominant subtype in adulthood (week 8): the ILC3-dominant category (small intestine in Figure 1A and 1B), the ILC2-dominant category(colon in Figure 1D and 1E, and lung in Figure S1A and S1B), and the ILC1-dominant category (spleen in Figure 1G and 1H, and liver in Figure S1D and S1E).

Despite the organ-specific variations in ILC subset distribution, a consistent

pattern emerged, marked by a higher percentage of lymphoid tissue inducer (LTi) cells during the fetal and neonatal stages, transitioning to an elevated abundance of non-LTi ILCs, i.e., ILC1s, ILC2s, and ILC3s, in adulthood (Figure 1B, 1E, and 1H, Figure S1B and S1E). Concurrently, the ratio of LTi cells to non-LTi ILCs exhibited a gradual decline across all examined organs, reaching a stable state around two weeks postnatally (Figure 1C, 1F, and 1I, Figure S1C and S1F). This consistent shift suggested a potential shared mechanism governing the dynamic alterations in ILC subsets throughout ontogeny.

Distinct progenitor differentiation capacity contributes to the composition shift of ILC subsets during ontogeny

While analysing ILCs, we also observed dynamic changes in αβT and γδT cells during ontogeny (Figure S2). Given the disparate capacities of hematopoietic progenitors to generate γδ T cells and αβ T cells during fetal and adult stages (Yuan et al., 2012), coupled with the close relationship between ILCs and T cells (De Obaldia and Bhandoola, 2015), we speculated that fetal and adult hematopoietic progenitors may exhibit differing abilities in generating LTi cells and non-LTi cells.

To investigate this hypothesis, we sorted hematopoietic progenitor cells (LSKs, $CD45^{+}Lin^{-}c\text{-}Kit^{+}Sca\text{-}1^{+}$) from fetal liver and adult bone marrow for an *in vivo* ILC differentiation assay. The resultant progenies in the small intestines of recipient mice were analyzed eight weeks later. Consistent with previous findings (Yuan et al., 2012), we observed a higher proportion of αβ T cells among the progenies derived from adult LSKs (Figure S3A). In contrast, the fetal LSK-derived cells exhibited higher proportions of ILCs and B cells (Figure S3A). Although both embryonic and adult LSKs exhibited proficiency in reconstituting all major ILC subsets (Figure S3B), a lower proportion of LTi cells and a higher abundance of ILC1s and ILC2s were identified among the ILCs derived from adult LSKs (Figure S3B and S3C), denoting an increased prevalence of non-LTi ILCs (Figure S3D). This observation aligned with the gradual reduction in the ratio of LTi cells to non-LTi ILCs throughout ontogeny.

To further compare the differentiation capacities of fetal and adult ILC progenitors, LSKs, CLPs, and αLPs were isolated from fetal liver and adult bone

159 marrow for an *in vitro* differentiation assay. As expected, fetal ILC progenitors
160 showed a predisposition for generating LTi cells (Figure S4A and S4C),
161 whereas their adult counterparts leaned towards producing ILC1s and ILC2s,
162 representing the non-LTi ILCs (Figure S4B and S4D). Furthermore, both fetal
163 and adult αLPs exhibited enhanced efficiency in ILC differentiation compared
164 to LSKs and CLPs (Figure S4C and S4D). Notably, a distinct population of
165 NCR^+ ILC3s was observed among the $ROR\gamma t^+$ ILCs derived from adult αLP2s,
166 whereas minimal to no NCR^+ ILC3s was generated by fetal αLP2s, during both
167 *in vitro* and *in vivo* differentiation assay (Figure S5). This divergence in ILC
168 composition derived from fetal and adult αLP2s precisely mirrored the distinct
169 distributions of ILC subsets between fetal and adult tissues.
170
171 Further analysis affirmed the consistent frequencies of CLPs, αLP1s, and
172 αLP2s throughout different ontogenic stages (Figure 2A and 2B). To identify
173 when the differentiation capacity begins to change, we sorted αLP2s from fetal
174 liver and bone marrow at different ages for an *in vitro* differentiation assay.
175 Remarkably, bone marrow αLP2s from mice within the first week post-birth
176 exhibited significant changes in differentiation ability, characterized by a
177 substantial decrease in the number of LTi cells and a simultaneous increase in
178 non-LTi ILCs, akin to adult αLP2s (Figure 2C to 2F). This observation suggested
179 that alterations in the differentiation capacity of ILC precursors occurred shortly
180 after birth, approximately one week prior to the establishment of a steady-state
181 in ILC subset composition across various tissues (Figure 1 and Figure S1).
182 Consequently, the postnatal shift in the differentiation ability of ILC precursors
183 could contribute to the dynamic changes of ILC subsets from the fetal to adult
184 stages.

185 Single-cell transcriptomic landscape of fetal and adult ILC 186 progenitors

187 ILC progenitors, rare populations in both fetal liver and adult bone marrow, have
188 not been thoroughly elucidated, particularly in fetal tissues. To address this gap,
189 we isolated αLPs, comprising both αLP1s and αLP2s, from fetal liver and adult
190 bone marrow for single-cell RNA sequencing (scRNA-seq) analysis. Following
191 stringent quality control procedures (see Methods), we selected 4284 fetal and
192 3442 adult αLPs for subsequent UMAP analysis. Ten distinct clusters were

193 revealed (Figure S6A), all expressing of *Ptprc*, *Il7r*, *Itga4*, and *Itgb7* (Figure
194 S6B). Clusters 0, 1, 2, and over half of cluster 6 exhibited high expression of
195 *Flt3*, representing αLP1s. Conversely, clusters not expressing *Flt3* represented
196 αLP2s (Figure S6B).
197
198 Based on the expression characteristics of known transcription factors, such
199 as *Id2*, *Tcf7*, and *Zbtb16*, we defined clusters associated with the ILC lineage,
200 specifically Cluster 6, 3, 7, 8, 9, and 4, primarily distributed within αLP2s (Figure
201 S6B). Notably, Clusters 6, 3, and 9 represented early-stage progenitors in ILC
202 development, evidenced by their high expression of *Tcf7*. A comparative
203 mapping analysis of cell transcriptome (Methods) revealed that these early
204 precursor cells shared some characteristics with early T cell progenitors (ETP)
205 and double-ngative (DN) T cells (Figure S6C). Among them, Cluster 6
206 expressed high *Nfil3* and low *Id2*, representing early ILC progenitors (EILPs)
207 (Harly et al., 2019). Cluster 3 showed high expression of *Zbtb16* and *Pdcd1*,
208 serving as specific markers for ILC progenitors (ILCPs) (Constantinides et al.,
209 2014; Yu et al., 2016). Additionally, Cluster 3 expressed signature genes of
210 multiple ILC subsets, including *Gata3*, *Rora*, *Ccl5*, *Ltb*, etc., leading us to define
211 it as ILCPs (Figure 3B). Cluster 7 also exhibited features of multiple ILC subsets,
212 and high *Il18r1* expression, indicative of ILCPs seeded in the peripheral tissues
213 via circulation system (Zeis et al., 2020), suggesting that Cluster 7 could
214 represent a later stage of ILCPs. Accordingly, we labeled Clusters 3 and 7 as
215 ILCP.1 and ILCP.2, respectively. Cluster 9, distinguished by high expression of
216 *Rorc*, *Cxcr5*, *Ccr6*, and *Ltb*, represented LTi precursors. Additionally, Cluster 9
217 highly expressed *Cd74*, *H2-Aa*, and *H2-Ab1*, possibly associated with the newly
218 annotated MHC-II^{+} LTi cells (Hepworth et al., 2013; Lyu et al., 2022). Meanwhile,
219 Cluster 4 exhibited high features of both LTi cells (*Ltb*, *Rorc*, etc.) and ILC2s
220 (*Gata3*, *Rora*, etc.) (Figure 3B), as confirmed by the cell-referring analysis
221 (Figure S6C). Since Cluster 4 showed low expression of *Tcf7* and *Il18r1* (Figure
222 3B), it might be a mixed cluster containing LTiPs and ILC2Ps at a more terminal
223 stage. Consequently, we defined Cluster 9 as an early stage LTiP.1 and Cluster
224 4 as LTiP.2/ILC2P. Finally, Cluster 8 was defined as NKPs based on their higher
225 expression of *Eomes*, *Tbx21*, *Il2rb*, etc. (Figure 3B and S6C).
226

227 Conversely, cells within Clusters 0, 1, 2, and 5, mainly comprising αLP1s, did
228 not exhibit significant genetic features of the ILC lineage. Cluster 0 showed high
229 expression of *Pbk* (Figure 3B), and a comparable fraction of Cluster 0 is
230 transcriptionally similar to pro-B cells (Figure S6C). Therefore, we defined
231 Cluster 0 as pro-B-like αLPs. Using the same strategy, we defined Cluster 1 as
232 CDP-like αLPs due to their high expression of *Irf8*, *Tcf4*, *Ctsh*, *Ctsb*, *Siglech*,
233 and Cluster 2 as ETP-like αLPs due to their high expression of *Cd34*, *Lmo2*,
234 *Egfl7* (Figure 3B and S6C). Cluster 5 exhibited a high degree of heterogeneity,
235 containing various cell types, and was labeled as early αLPs due to its early
236 developmental characteristics (Figure 3B and S6C). Cluster 5 exhibited high
237 expression of genes shared by Cluster 0, 1, 2, and 6, and contained multiple
238 cell types, representing the highest heterogeneity among all these clusters
239 according to cell referring analysis (Figure 3B and S6C). Therefore, we define
240 Cluster 5 as the early αLPs.
241
242 Among the ten identified clusters, we observed an even distribution of cells
243 from fetal liver and adult bone marrow, except for Cluster 4 (LTiP.2/ILC2P)
244 (Figure 3C). Notably, fetal Cluster 4 was annotated as LTi cells, while adult
245 Cluster 4 is annotated as ILC2, based on cell referring analysis (Figure S6D).
246 Furthermore, fetal Cluster 4 showed higher expression of *Rorc*, *Cxcr5*, *Ccr6*,
247 etc., indicating the LTiP moiety (Figure S6E), whereas adult Cluster 4 exhibited
248 higher expression of *Rora*, *Gata3*, *Bcl11b*, *Il17rb*, etc., consistent with ILC2P
249 characteristics (Figure S6G). Consequently, we refined the annotation, defining
250 fetal Cluster 4 as LTiP.2 (Figure S6F) and adult Cluster 4 as ILC2P (Figure S6H).

251 RNA velocity analysis predictes a conserved ILC differentiation 252 trajectory in fetal liver and adult bone marrow

253 The markedly different capacity of fetal and adult ILC progenitors implicated
254 potential distinct developmental pathways underlie these two stages. To further
255 investigate this hypothesis, we employed RNA velocity analysis (Methods) to
256 predict differentiation trajectories in both fetal and adult αLPs.
257
258 Four relatively conserved differentiation trajectories were predicted for both
259 fetal and adult αLPs, all originating at early αLP (C5) and branching towards
260 pro-B-like αLP (Cluster 0, Path 0), CDP-like αLP (Cluster 1, Path 1), ETP-like

αLP (Cluster 2, Path 2), and ILC lineage (Cluster 3, Path 3), respectively (Figure 3D to 3F). Notably, a conserved ILC lineage (Path 3), initiated from early αLP (C5) and extending through EILP (C6) and ILCP (C3), was identified in both fetal liver and adult bone marrow. However, this ILC lineage (Path 3) terminated as LTiP in fetal liver, while transitioning to ILC2P in adult bone marrow (Figure 3D to 3F). This observation suggested that crucial regulatory factors may have undergone alterations from fetal to adult ILC development, resulting in distinct progenies of ILC progenitors despite the apparently conserved developmental pathway.

RORγt- and GATA3-biased gene programs in fetal and adult ILC subset fates

To further explore the gene regulatory networks governing fetal and adult ILC development, we identified activated gene modules by applying the TSC (temporal spatial consensus) algorithm as described in the Method sections. We selected representative cells from the four trajectories (Figure 4A), analyzed the gene expression dynamics of these cells along Path 3, which represents the ILC commitment path from C5 to C3 (Figure 4B), and proposed a set of key gene regulatory modules along the path (Figure S7). Consistent with the conserved trajectories in both fetal and adult ILC development, we observed common patterns in gene expression dynamics. For example, we found that genes including *Flt3*, *Spi1*, *Irf8*, and *Lmo2* were notably enriched in the early stage of pseudotime, showing a significant decrease as differentiation progressed (Figure 4B). Following this, the induction of *Lck*, *Sox4*, *Tcf7*, and *Gfi1b* expressions marked the initiation of ILC commitment from early progenitor cells. This initiation was accompanied by the following expression of *Tox*, *Id2*, and *Zbtb16*, which further restricted the ILC commitment in these progenitors (Figure 4B).

Nevertheless, the gene expression programs had exhibited major different logic between the fetal and adult stages. Specifically, in the fetal stage, we observed that the expression of *Rorc* was nearly synchronous with *Tox* and *Id2*, whereas the *Gata3* expression was relatively delayed (Figure 4B and S7A). Conversely, in the adult stage, the *Gata3* expression closely paralleled that of *Tox*, *Id2*, and *Zbtb16*, whereas the peak expression of *Rorc* lagged behind

295 (Figure 4B and S7B). Moreover, our analysis of differentially expressed genes
296 revealed elevated expression levels of *Gata3* and *Bcl11b* in the adult clusters,
297 particularly in C6 (EILP) and C3 (ILCP), but higher *Id2* and *Rorc* in the fetal
298 clusters (Figure S8A). Additionally, higher GATA3 expression in adult ILCPs (C3:
299 GATA3^{hi}TCF-1^{+} αLP2) and lower RORγt in the adult clusters (C9: RORγt^{hi} TCF-
300 1^{+} αLP2) were confirmed by the flow cytometry analyses (Figure S8D to S8F).
301 Consistent with these findings, the expression level of RORγt in intestinal
302 RORγt^{+} ILCs gradually decreased during the ontogeny (Figure S8G and S8H).
303
304 Notch signaling plays a crucial role in ILC differentiation, especially the ILC2s
305 and ILC3s (Possot et al., 2011; Wong et al., 2012). Notably, we observed that
306 *Notch2* was transiently expressed in the early stage of fetal ILC lineage (Path
307 3), followed with a significant downregulation. Conversely, in the adult stage,
308 *Notch2* expression nearly synchronized with *Zbtb16* and *Gata3* (Figure 4B).
309 Moreover, *Rbpj*, a pivotal downstream component of the Notch receptor, was
310 also synchronously expressed with *Tox* and *Id2* during adult ILC commitment
311 (Figure S7B), in contrast to its limited temporal expression during fetal ILC
312 commitment (Figure S7A). Our analyses of differentially expressed genes
313 uncovered elevated expression levels of *Notch1* and *Rbpj* in adult clusters
314 (Figure S8A). Additionally, higher Notch2 expression in adult αLPs was
315 confirmed by flow cytometry analysis (Figure S8B and S8C). Gene Set Variation
316 Analysis (GSVA) further indicated a notably enriched Notch signaling pathway
317 in adult αLPs (Figure S9). Consequently, a heightened level of Notch signaling
318 activity was discerned during ILC development in the adult stage than in the
319 fetal stage.
320
321 The induction of GATA3 and Bcl11b as a consequence of Notch signaling
322 activation has been documented in previous studies (Ho et al., 2009; Hosokawa
323 and Rothenberg, 2021; Rothenberg, 2019). These factors are known to exert
324 repression on *Rorc* expression (Califano et al., 2015; Zhong et al., 2015).
325 During adult ILC commitment, we observed an elevation in the expression of
326 *Gata3* and *Bcl11b* (C6 and C3), closely following the heightened expression of
327 *Notch1*, *Notch2*, and *Rbpj* (C5), key components of the Notch signaling pathway.
328 This trend was less apparent during fetal ILC development (Figure 4C).

329 Additionally, an evident opposing expression pattern between *Gata3*/*Bcl11b*
330 and *Rorc* became apparent. Elevated *Gata3* and *Bcl11b* expression aligned
331 with decreased *Rorc* expression during adult ILC commitment. Conversely,
332 elevated *Rorc* expression was associated with decreased *Gata3* and *Bcl11b*
333 during fetal ILC commitment (Figure 4C).
334
335 Furthermore, we quantified the activation levels of the Notch signaling
336 pathway, the GATA3 regulon, and the RORγt regulon during ILC differentiation
337 as well as their mutual regulations (Method). We employed ternary plots to
338 analyze the interplay between them, as depicted in Figure 4D. The cell states
339 (points on the ternary plots) shifted from a RORγt-dominant distribution (fetal)
340 to a Gata3-Notch dominant distribution (adult). These data suggested that
341 RORγt may act as a key transcription factor during fetal ILC development,
342 whereas Notch signaling and GATA3 appear to be more influential in
343 modulating adult ILC development. With the help of *dynamo* analysis (Qiu et
344 al., 2022), we further predicted a suppressive effect of GATA3 and Bcl11b on
345 *Rorc* expression, particularly in the adult ILCP (C3) (Figure 4E and 4F). The
346 analysis calculated Jacobian values for each cell and reported negative partial
347 derivatives in the ILCP zones on the UMAP.
348
349 Based on the above observations and previously reported discoveries, we
350 inferred a regulatory model that explains the ILC subset preferences during
351 fetal and adult stages. In this model, we suggested that the amplified Notch
352 signaling observed in adulthood likely leads to an upregulation of GATA3 and
353 Bcl11b. This in turn results in the downregulation of Rorc expression, as
354 detailed in Figure 4G.

355 Enhanced activity of Notch-GATA3-signaling suppresses the 356 generation of LTi cells but promotes non-LTi ILCs

357 Given the pivotal roles of Notch signaling, GATA3, and RORγt in the
358 developmental process of ILCs (Chea et al., 2016b; Cherrier et al., 2012; Eberl
359 et al., 2004; Possot et al., 2011; Sanos et al., 2009; Vonarbourg et al., 2010;
360 Yagi et al., 2014; Zhong et al., 2015; Zhong et al., 2020), we speculated that
361 changed Notch signaling, GATA3 and RORγt expression may result in the
362 modified fate determination of ILC subsets from the fetal to the adult stage.

363

364 To address this question, we performed an *in vitro* differentiation assay of
365 ILCs using the OP9-DL1 cell line as feeder cells, which provides continuous
366 ligands for activation of Notch signaling. Our experiments found that sustained
367 activation of Notch signaling led to a substantial increase in the proportion of
368 ILC2s (Figure 5A), which was consistent with prior studies (Wong et al., 2012).
369 The ILC2s increase was acompanied by a significant reduction in the proportion
370 of LTi cells among the progenies of fetal ILC progenitors (Figure 5B) and a
371 notable decrease in the proportion of ILC1s among the progenies of adult ILC
372 progenitors (Figure 5C). The proportion of ILC3s exhibited no significant
373 change during this process (Figure 5D). Thus, enhanced Notch signaling
374 promoted the generation of ILC2 while suppressing LTi cell development. This
375 phenomenon could explain why the ILC lineage in the fetal liver ended with
376 LTiPs, while in adult bone marrow with ILC2Ps (Figure 3D to 3F). Moreover,
377 intervening in Notch signaling by DAPT at early stages, such as CLP and αLP1,
378 resulted in a more substantial alteration of ILC subsets (Figure 5A to 5D).
379 Additionally, blocking Notch signaling in αLP2s could significantly reduced their
380 ability to differentiate into ILC3s, leading to the decreased proportion of ILC3s
381 and increased proportion of LTi cells (Figure S10). However, this intervention
382 had limited effects on the generation of ILC1s and ILC2s (Figure S10).

383

384 To assess the impact of elevated GATA3 expression on ILC differentiation
385 from fetal to adult stage, we conducted *Gata3* overexpression experiments in
386 fetal hematopoietic stem/progenitor cells (HSPCs). Subsequently, these
387 modified HSPCs were then transplanted into recipient mice to observe *in vivo*
388 ILC differentiation. Analysis of the progenies derived from GATA3-
389 overexpressing HSPCs revealed a significant increase in the porpportion of
390 ILC2s, accompanied by a notable decrease in the proportion of total RORγt$^+$
391 ILCs. Within the RORγt$^+$ ILCs, Gata3 overexpression led to an increased
392 proportion of NCR$^+$ ILC3s and a decreased proportion of LTi cells (Figure 5E to
393 5G). Furthermore, *Gata3* overexpression resulted in a reduction in the
394 expression level of RORγt in RORγt$^+$ ILCs isolated from the recipient small
395 intestine (Figure 5H and 5I). This observation aligned with the previously

396 established negative regulatory effect of GATA3 on *Rorc* expression (Figure 4E
397 to 4G).
398
399 The reduced RORγt expression, as shown in adult *Rorc* heterozygous mice
400 with both *Rorc*$^{Gfp/+}$ and *Zbtb16*^{Cre}*Rorc*$^{f/+}$ genotypes (Figure 5K and 5L), led to
401 decreased proportion of LTi cells among RORγt^{+}ILCs and substantially
402 increased proportion of NCR^{+}ILC3s (Figure 5J and 5N). However, the
403 proportions of ILC1s and ILC2s showed no significant change in *Rorc*
404 heterozygous mice (Figure 5J and 5M). Additionally, upon transplanting the
405 LSKs from the adult *Rorc* heterozygous mice for *in vivo* ILC differentiation
406 analysis, we found a dramatically decreased proportion of total RORγt^{+}ILCs.
407 Within this population, the proportion of LTi cells was significantly reduced,
408 while the proportion of NCR^{+}ILC3s showed a remarkable increase (Figure S11A
409 and S11B).
410
411 Furthermore, we observed that NCR^{+}ILC3s emerged three days after birth
412 in the small intestine of *Rorc*$^{Gfp/+}$ mice, a significantly earlier occurrence
413 compared to wild-type mice (Figure S11C). This observation indicated an
414 accelerated induction of NCR^{+}ILC3s in mice when the RORγt expression level
415 was halved. Notably, an increased proportion of the NCR^{+}ILC3 population was
416 also generated by fetal liver αLPs from *Rorc*$^{Gfp/+}$ mice, compared to that derived
417 from wild type fetal αLPs (Figure S11D and S11E). Additionally, an elevated
418 proportion of NCR^{+}ILC3s and a reduction in LTi cells were detected among the
419 progenies of adult *Rorc* heterozygous αLP2s (Figure S11F and S11G). In
420 contrast, upon further overexpressing RORγt in adult hematopoitic
421 stem/progenitor cells (HSPCs), a decreased proportion of NCR^{+}ILC3s and an
422 increased proportion of LTi cells were observed among the progenies in the
423 recipient small intestine, while the development of ILC1s and ILC2s remained
424 largely unaffected (Figure S11H to S11L).
425
426 Taken together, these findings demonstrated a hierarchical molecular
427 regulation of ILC differentiation throughout mouse ontogeny. Specifically, a
428 higher level of RORγt expression by fetal ILC progenitors correlated with an
429 increased potential to preferentially generate LTi cells, particularly during the

fetal and neonatal stages. Conversely, enhanced Notch-GATA3 signaling in the ILC precursors during later developmental stages was associated with decreased RORγt expression, fostering the generation of non-LTi ILCs while suppressing LTi cell production. Consequently, the dynamic modulation in the fate of different ILC subsets during ontogeny appears to be driven by a seesaw-like transition: moving from a RORγt-dominant phase in fetal stages to a stage characterized by enhanced Notch signaling and GATA3 in adulthood.

DISCUSSION

ILCs play a crucial role in maintaining tissue homeostasis within the immune system, with different subsets mediating distinct immune response (Bal et al., 2020; Vivier et al., 2018). Dynamic alterations in ILC subsets have been documented in the murine small intestine (Sawa et al., 2010) and thymus (Jones et al., 2018) in recent years. However, a comprehensive elucidation of this phenomenon across various tissues during ontogeny is yet to be achieved. In this study, we proposed a “seesaw” model of the interplay between Notch-GATA3 signaling and RORγt during murine ontogeny. Specifically, RORγt demonstrated enhanced regulatory influence in fetal ILC development, whereas the Notch signaling pathway and GATA3 assumed augmented regulatory functions in adulthood. This model elucidated the predisposition of fetal ILC progenitors towards LTi cell differentiation, contrasting with the preference of non-LTi ILCs exhibited by adult progenitors. This dynamic regulation of ILC progenitors may account for the evolving composition of ILCs during ontogeny.

It is reasonable that different ILC subsets are required during various developmental stages. Remarkably, our findings, along with those of others, consistently demonstrate a prevalence of LTi cells throughout fetal and newborn tissues, followed by an increased proportion of non-LTi ILCs, including ILC1s, ILC2s, and ILC3s. The significant role of LTi cells in the formation of secondary lymphoid organs (Eberl et al., 2004; Krishnamurty and Turley, 2020), particularly during the embryonic and newborn stages (Onder and Ludewig, 2018), suggests a prioritization in the body to establish key secondary lymphoid tissues in anticipation of the impending immune defense post-birth. However,

with the direct exposure to various pathogens after birth, non-LTi ILCs become critical to defense against various pathogens (Eberl et al., 2015; Lim and Di Santo, 2019; Oherle et al., 2020; Vivier et al., 2018), particularly during the early stages after birth, when the T cell-mediated adaptive immune response is incompletely formed (Mao et al., 2018).

Recent studies have emphasized the impact of local niches on this process (Lim et al., 2017; Oherle et al., 2020; Zeis et al., 2020). For instance, a high concentration of AhR ligands in the small intestine promotes the differentiation and proliferation of ILC3s while restricting the expansion of ILC2s (Kiss et al., 2011; Lee et al., 2012; Li et al., 2018). In the lung environment, regardless of whether these precursor cells originate from neonatal or adult sources, they are driven to differentiate into ILC2s (Ghaedi et al., 2020; Oherle et al., 2020; Zeis et al., 2020). However, these findings could not fully explain the phenomenon observed in this study, where the ratio of LTi cells to non-LTi ILCs systematically decreased across tissues during ontogeny. Therefore, additional mechanisms regulating the dynamic changes of ILC subset composition require further clarification.

It is well-established that the characteristics of hematopoietic stem/progenitor cells (HSPCs) change during ontogeny (Jassinskaja et al., 2017; Kim et al., 2007; Medvinsky et al., 2011; Yuan et al., 2012). Fetal HSPCs exhibit a higher capacity of $\gamma\delta$ T cells generation, while adult HSPCs show an enhanced capacity of αβ T cells generation (Yuan et al., 2012). Correspondingly, fetal tissues manifest a higher composition of $\gamma\delta$ T cells, whereas adult tissues exhibit a higher proportion of αβ T cells (Dunon et al., 1997). In line with the widely shared regulatory mechanisms governing T cell and ILC development, our findings demonstrate distinct capacities for generating ILC subsets from fetal and adult hematopoietic progenitors. Particularly noteworthy is the higher capacity for LTi cell generation by fetal progenitors, contrasting with the greater capacity for non-LTi ILC generation by adult progenitors. This pattern aligns with the systematic reduction in the ratio of LTi cell to non-LTi ILC from the fetal to adult development. Therefore, we propose that hematopoietic progenitors, exhibiting distinct differentiation capacities for ILC subsets at different

497 developmental stages, play a significant role in driving the dynamic changes in
498 ILC subset composition during ontogeny.
499
500 A series of ILC progenitors has been identified in adult bone marrow (De
501 Obaldia and Bhandoola, 2015; Harly et al., 2019; Ren et al., 2022; Vivier et al.,
502 2018), however, there is still a lack of comprehensive profiling of ILC
503 progenitors during fetal development (Ishizuka et al., 2016). Notably, the
504 development of fetal and adult ILCs exhibits distinct sensitivities to the
505 deficiency of Notch signaling (Chea et al., 2016a; Possot et al., 2011) and
506 Ikaros (Li et al., 2016; Schjerven, 2013), implying potential different ILC
507 developmental pathways between these two stages. Contrary to expectations,
508 our scRNA-seq analyses revealed similar types of ILC progenitors and a
509 conserved differentiation trajectory during fetal and adult ILC development.
510 However, fetal and adult progenitors exhibited different transcriptomes and
511 gene regulatory networks. Remarkably, Notch signaling was enriched during
512 adult ILC development, as evidenced by higher expression of *Gata3*, *Tcf7*, and
513 *Bcl11b*. These transcription factors, involved in ILC subset fate determination,
514 are all known to be promoted by Notch signaling (Cherrier et al., 2018; Fang
515 and Zhu, 2017). Moreover, TCF-1 (encoded by *Tcf7*) (Mielke et al., 2013; Yang
516 et al., 2015), GATA3 (Zhong et al., 2016; Zhong et al., 2020) and Bcl11b
517 (Califano et al., 2015) all show a higher requirement for non-LTi ILC generation,
518 concurrently suppressing LTi cell differentiation. This aligns with the
519 observation that adult ILC3s, not fetal LTi cells, depend on Notch signaling
520 (Chea et al., 2016a; Possot et al., 2011). Consistent with prior observations that
521 GATA3 and Bcl11b can suppress RORγt expression (Califano et al., 2015;
522 Zhong et al., 2020), we aso confirmed reduced RORγt expression in the adult.
523 Moreover, reduced RORγt expression accelerated the emergence of ILC3 and
524 suppressed LTi cell generation. Therefore, we propose the modified activity of
525 Notch signaling, leading to changed expression of Gata3 and Rorc, will altered
526 the fate determination of ILC subsets and ultimately contribute to the dynamic
527 change of ILC subsets during ontogeny.
528
529 Furthermore, Notch signaling also plays a role in determining the fate of αβ
530 T cells and γδ T cells in a dose-dependent manner. Increased Notch signaling

activity is necessary for the generation of αβ T cells, while it is not essential for γδ T cells (Ciofani et al., 2006; Garbe et al., 2006; Tanigaki et al., 2004). Taking into account the enhanced Notch signaling observed in adult ILC progenitors, which still maintain T cell differentiation capacity, exemplified by the early αLP1 cluster (C5) we identified, it is plausible that enhanced Notch signaling could serve as a common trigger for shifting differentiation capacity from LTi cells to non-LTi ILCs, and probably from γδ T cells to αβ T cells as well, during the transition from fetal to adult stages. However, the mechanisms underlying the modulation of Notch signaling strength during ontogeny remain unclear and warrant further investigation.

Collectively, our findinngs highlight the dynamic regulation of ILC subset fate determination by adjusting the activity of Notch-GATA3 signaling and RORγt expression, leading to the gradually decreased ratio of LTi cells to non-LTi ILCs from fetal to adult. This study propose an additional mechanism that altered differentiation capacity of ILC progenitors may coordinate with the environment cues to meet the demands of distinct ILC subsets in the body during mouse ontogeny.

Limitations of Study

Our study revealed a correlation between changes in the differentiation ability of ILC progenitor cells and the dynamic composition of ILC subsets in tissues during ontogeny. However, direct evidence for the extent to which changes in differentiation ability contribute to the distribution of ILC subsets in peripheral tissues is lacking. While we demonstrated that the differentiation capacity of ILC progenitors changed as early as one week after birth, we were unable to determine definitively whether ILC progenitors from the bone marrow are still required for generating ILC subsets in peripheral tissues after birth. This consideration is particularly pertinent given the tissue-residence feature of ILCs in adults.

AUTHOR CONTIBUTIONS

T.W., S.C., and L.W. designed the study. T.W. performed the experiments and acquired data with assistance of X.Zhu. S.C. analyzed the single-cell RNA-seq data. Y.Z., J.M., and J.Z. provide the single-cell RNA-seq data. M.L., Y.T., Q.S., X.G. and Y.W. provided

technical and experimental assistance. T.W., S.C., L.W. analyzed and interpreted the data. Manuscript was written by T.W., S.C. and L.W., S.C. and J.M. are responsible for the data curation, and this study was supervised by L.W., Y.Z. and X.Zhang.

ACKNOWLEDGEMENTS

We thank Xiaoguang Li, Wenlong Lai, Yujie Tian, Yijun Zhang, Jiaoyan Lv, Xin Liu, Chao Wang, Zen Shi, Site Feng, Haoxiang Gao, Ning Wu and Jingjiao Wu for for administrative/support. We thank Qinli Sun from Dr. Chen Dong lab in this institute for providing the *Rorc* over-expression plasmid. We thank Dr. Yan Shi, Dr. Xiaoyu Hu and Dr. Wenwen Zeng for providing advice. Flow cytometry and cell sorting were carried out on IITU platforms. We also thank the assistance of Laboratory Animal Research Center of Tsinghua University. This study was supported by grants from the Ministry of Science and Technology of China (National Key Research Project: 2019YFA0508502 and 2022YFC2505001 to L.W.; 2020YFE0202200 to Y.Z. and J.M.; 2021YFF1200900 to X.Z.), the National Natural Science Foundation of China (Grants 31991174 to L.W.; Grant 62250005 to X.Z.), the National Basic Research Center of China (82388101 to L.W.), China Postdoctoral Science Foundation (2022M721818 to T.W.) and Tsinghua-Peking Center for Life Sciences (to L.W. and T.W.).

DECLARATION OF INTERESTS

METHODS

KEY RESOURCE TABLE

RREGENT or RESOURCE	SOURCE	IDENTIFIER
Antibodies		
Anti-mouse CD45 BV605 (30-F11)	BioLegend	Cat# 103112
Anti-mouse CD45.1 BV605 (A20)	BioLegend	Cat# 110738
Anti-mouse CD45.1 BV711 (A20)	BioLegend	Cat# 110739
Anti-mouse CD45.1 V450 (A20)	BD Biosciences	Cat# 580520
Anti-mouse CD45.2 PE-Cy7 (104)	BioLegend	Cat# 109830
Anti-mouse CD45.2 APC (104)	BioLegend	Cat# 109814
Anti-mouse CD45.2 APC-Cy7 (104)	BioLegend	Cat# 109824
Anti-mouse CD45.2 FITC (104)	Thermo Fisher Scientific	Cat# 11-0454-85
Anti-mouse CD3ε FITC (145-2C11)	BioLegend	Cat# 100306
Anti-mouse CD4 BV711 (RM4-5)	BioLegend	Cat# 100550
Anti-mouse CD8α APC-Cy7 (53-6.7)	BioLegend	Cat# 100714
Anti-mouse TCR-β FITC (H57-597)	Thermo Fisher Scientific	Cat# 11-5961-85
Anti-mouse CD11b FITC (M1/70)	Thermo Fisher Scientific	Cat# 11-0122-85

Anti-mouse CD11c FITC (N418)	Thermo Fisher Scientific	Cat# 11-0114-85
Anti-mouse CD11b PerCP/Cy5.5 (M1/70)	BD Biosciences	Cat# 550993
Anti-mouse CD19 FITC (6D5)	BioLegend	Cat# 115505
Anti-mouse NK1.1 APC (PK136)	Thermo Fisher Scientific	Cat# 17-5941-82
Anti-mouse NKp46 PerCP-eF710 (29A1.4)	Thermo Fisher Scientific	Cat# 46-3351-82
Anti-mouse NKp46 PE-Cy7 (29A1.4)	Thermo Fisher Scientific	Cat# 25-3351-82
Anti-mouse Thy1.2 APC-Cy7 (30-H12)	BioLegend	Cat# 105328
Anti-mouse Thy1.2 APC-eFluor780 (53-2.1)	Thermo Fisher Scientific	Cat# 47-0902-82
Anti-mouse GATA3 eFluor660 (TWAJ)	Thermo Fisher Scientific	Cat# 50-9966-41
Anti-mouse RORγt PE (AFKJS-9)	Thermo Fisher Scientific	Cat# 12-6988-82
Anti-mouse CCR6 BV421 (29-2L17)	BioLegend	Cat# 129818
Anti-mouse c-Kit APC-Cy7 (ACK2)	BioLegend	Cat# 135136
Anti-mouse c-Kit BV605 (ACK2)	BioLegend	Cat# 135121
Anti-mouse c-Kit APC (ACK2)	Thermo Fisher Scientific	Cat# 17-1172-83
Anti-mouse CD127-biotin (A7R34)	Thermo Fisher Scientific	Cat# 1312721-82
Anti-mouse CD127-BV421 (A7R34)	BioLegend	Cat# 135024
Anti-mouse $\alpha_4\beta_7$ APC (DATK-32)	Thermo Fisher Scientific	Cat# 17-5887-82
Anti-mouse $\alpha_4\beta_7$ PE (DATK-32)	Thermo Fisher Scientific	Cat# 12-5887-83
Anti-mouse Flt3 PE (A2F10)	Thermo Fisher Scientific	Cat# 12-1351-82
Anti-mouse Flt3 BV421 (A2F10)	BioLegend	Cat# 135314
Anti-mouse CD25 BV711 (PC61)	BioLegend	Cat# 102049
Anti-mouse Notch1 PE (HMN1-12)	BioLegend	Cat# 130607
Anti-mouse Notch2 PE (HMN2-35)	BioLegend	Cat# 130707
Anti-mouse KLRG-1 BV605 (2F1/KLRG1)	BioLegend	Cat# 138419
Anti-mouse KLRG-1 APC (2F1/KLRG1)	BioLegend	Cat# 138412
Ki-67-PE-Cy7 (SolA15)	Thermo Fisher Scientific	Cat# 25-5698-82
Chemicals, peptides, and recombinant proteins		
Recombinant Murine IL-7	PeproTech	Cat# 217-17
Recombinant Murine SCF	PeproTech	Cat# 250-03
Recombinant Murine Flt3L	PeproTech	Cat# 250-31L
DAPT	Selleck	Cat# S2215
Collagenase Type III	Worthington Chemicals	Cat# CLS-3
Penicillin- Streptomycin (10,000 U/mL)	GIBCO	Cat# 15140122
Percoll	GE Healthcare	Cat# 17-0891-01
RPMI 1640	GIBCO	Cat# C22400500BT
HBSS	GIBCO	Cat# C14175500CP
Critical commercial assays		
Foxp3 transcription factor staining buffer set	Thermo Fisher Scientific	Cat# 00-5523-00
BioMag anti-Rat IgG	Bangs Laboratories	Cat# BM560

7-AAD	Thermo Fisher Scientific	Cat# 00-6993-50
Flexible viability dye eFulor506	Thermo Fisher Scientific	Cat# 65-0866-18
Rat Gamma Globulin	Jacksonimmuno	Cat# 012-000-002
Experimental Models: Organisms/Strains		
C57BL/6J mice	Jackson lab	Jax000664 Jax002014
Rorc$^{GFP/+}$ mice	Dr. Xiaohuan Guo	N/A
Rorc$^{-/-}$*Il2rg*$^{-/-}$ mice	Dr. Xiaohuan Guo	N/A
Zbtb16^{Cre} mice	Dr. Xiaohuan Guo	N/A
Rorc$^{f/+}$*Zbtb16*^{Cre} mice	Dr. Xiaohuan Guo	N/A
OP9 cell line	Dr. Xiaohuan Guo	N/A
OP9-DL1 cell line	Dr. Xiaohuan Guo	N/A
pMSCV[Exp]-mGata3[NM_008091.3]:IRES:EGFP	VectorBuilder	
Software and algorithms		
FACS Diva software	BD Biosciences	
FlowJo V9.9.3 software	TreeStar	
GraphPad Prism 7.0 software	GraphPad	

RESOURCE AVAILABILITY

Lead contact

Further information and requests for resources and reagents should be directed to and will be fulfilled by the lead contact, Li Wu (wuli@tsinghua.edu.cn).

Materials availability

This study did not generate any new unique reagents.

Data and code availability

Single-cell RNA-seq data have been deposited at GSA (https://ngdc.cncb.ac.cn/gsa/) with the accession number CRA011319. The codes for scRNA-seq data analysis were available at an online repository (https://github.com/chansigit/ilcdev).

EXPERIMENTAL MODEL AND SUBJECT DETAILS

Animals and ethics statement

CD45.2 mice (Jax000664) and CD45.1 mice (Jax002014) were obtained from Jackson Laboratory. CD45.1.2 mice were generated by crossing CD45.2 mice (Jax000664) and CD45.1 mice (Jax002014). *Rag2*$^{-/-}$*Il2rg*$^{-/-}$ mice, *Rorc*$^{GFP/+}$ mice, *Zbtb16*^{Cre} mice, *Rorc*$^{f/+}$*Zbtb16*^{Cre} mice were kindly provided by Dr. Xiaohuan Guo (Tsinghua University, Beijing, China). Mouse embryos and pups were obtained by in-house breeding. Age of mice were illustrated in indicated experiment. Fetal liver were collected at embryonic day 15.5 (E15.5) or E16.5. For adult bone marrow analysis, 8- to 12-week-old mice were used. Mice after two weeks old were sex-matched, while the male and female fetus or newborn mice were randomly used.

605 All mice used in this study were bred on a C57BL/6 background, and maintained in a specific
606 pathogen free (SPF) animal facility (12 h light and 12 h dark) at Tsinghua University. Animal
607 procedures were under the approval of the Institution Animal Care and Use Committee at
608 Tsinghua University.

609 METHOD DETAILS

610 Cell preparation

611 Single-cell suspensions of bone marrow, fetal liver, small intestine, colon, lung, spleen and
612 liver were prepared following the listed protocols for flow cytometry analysis and/or cell
613 sorting.

614 For progenitor enrichment from bone marrow, procedures were detailly described
615 elsewhere (Manz et al., 2001; Wu et al., 2001). Briefly, bone marrow cells were enriched
616 by red blood cell removing, density gradient centrifugation (1.086 g/ml Nycodenz), and
617 immunomagnetic depletion of the lineage positive cells labeled by markers of CD3, CD2,
618 CD8, CD19, B220, Mac-1, Ly6G and Ter119. For cell isolation from fetal liver, fetal liver
619 was collected from E15.5 or E16.5 fetus and repeatedly blew by 1 ml pipette tip, cell
620 suspensions were passed through a 70 μM strainer, further enriched by red cell removing
621 and density gradient centrifugation (1.086 g/ml Nycodenz), cells that lighter than 1.086
622 g/ml were collected and washed. These enriched cells were blocked by Rat IgG and further
623 stained with indicated antibody panel for CLPs ($Lin^{-}CD127^{+}c\text{-}Kit^{int/+}Flt3^{+}\alpha_4\beta_7^{-}$), αLP1s
624 ($Lin^{-}CD127^{+}c\text{-}Kit^{int/+}Flt3^{+}\alpha_4\beta_7^{+}$), αLP2s ($Lin^{-}CD127^{+}c\text{-}Kit^{int/+}Flt3^{-}\alpha_4\beta_7^{+}$).

625 For cell isolation from the small intestine and colon, the small intestine and colon were
626 flushed clean with cold mouse tissue PBS, opened along the longitudinal axis, and then
627 removed the Peyer's patches. The residual intestinal tissues were subjected to two
628 sequential 20-min incubated in 20 ml Buffer I (HBSS with 20mM EDTA, 10mM HEPES and
629 1M DTT), at 37℃ with shaking (220 rpm), for the preliminary digestion. Peyer's patches
630 and mesenteric tissues were removed from the residual intestinal tissues that were further
631 incubated in 10 ml Buffer II (1640 RPMI + 10% FBS + 1mg/ml Collagenase III) for 60min
632 at 37℃ with shaking (220 rpm), for final digestion. After which, samples were violently
633 vortexed, repeatedly blew by 1 ml pipette tips, and then passed through 70 μM strainer,
634 40% Percoll density gradient centrifugation was used for further immune cells enrichment.
635 The cells that heavier than 40% Percoll were washed and counted for further analysis.

636 For lung cell isolation, mouse lung tissues were minced and digested with collagenase
637 1A (0.5 mg/ml, Sigma) and Dnase I (0.05 mg/ml, Roche) in HBSS for 60 minutes at 37℃
638 in the thermostatic incubator, with several interval vortexes. Digested lung tissues were
639 further filtrated through a 70 μM strainer, the erythrocytes were removed by using red cell
640 removal buffer (0.168M NH_4CL), the residual cells were washed and collected for further
641 analysis.

642 For liver cell isolation from mice after birth, livers were collected and passed through a
643 100 μM strainer. The cells then enriched by density gradient centrifugation with 40%
644 Percoll, and red blood cells were removed. Splenocytes were isolated by forcing the
645 tissues through a 100 μM strainer, and red blood cells were further removed.

646 Flow cytometry analysis and cell sorting

647 Flow cytometry staining were performed in 96-well microtiter plates or 5 ml FACS tube.
648 Cells were blocked by Rat IgG and stained with fluorochrome-conjugated antibodies in
649 dark for 30-40 min on ice. Fixable Viability Dye eFluor506 or 7-AAD were used to exclude
650 the dead cells in all these samples. For intracellular transcription factor staining, cells were
651 fixed and permeabilized and stained with indicated antibodies using the
652 Foxp3/Transcription Factor Staining Buffer Set (Thermo Fisher Scientific). Data were
653 acquired on a BD LSRII or Fortessa cytometer, and cells were sorted by FACSAria III, in
654 the flow cytometry core at IITU.

655 ***In vitro* differentiation assay of ILC progenitors**

656 We cultured bone marrow progenitors (0.5-1×10^4/sample) from CD45.1 or CD45.2 wild
657 type mice, including CLP, αLP1, and αLP2, with total bone marrow cells (1×10^4/sample)
658 from CD45.1.2 wild type or CD45.2 *Rag2*$^{-/-}$*Il2rg*$^{-/-}$ mice as feeder cells in RPMI 1640
659 media supplemented with 10% fetal bovine serum, glutamine, β-mercaptoethanol,
660 penicillin, and streptomycin. For the OP9 and OP9-DL1 co-culture system, we sorted ILC
661 progenitors (500-1000 cells) and seeded them in wells with OP9 or OP9-DL1 cell lines
662 (500 cells for each well). All cultures were supplemented with stem cell factor (SCF, 100
663 ng/ml) and IL-7 (20 ng/ml), and ILC subsets among the daughter cells were analyzed 7-8
664 days later by flow cytometry.

665 **Adoptive transfer of ILC progenitors for in vivo differentiation assay**

666 We sorted equal number (0.5~1×10^4 for one recipient) of indicated progenitor from fetal liver
667 (CD45.2 wild type) and adult bone marrow (CD45.1,wild type mice), and mixed them with
668 competitor cells (5×10^5 for one recipient, total bone marrow from CD45.1.2 wild type or CD45.2
669 *Rag2*$^{-/-}$*Il2rg*$^{-/-}$ mice) befor transferring them to the lethally irradiated mice (CD45.1.2 wild type
670 or CD45.2 *Rag2*$^{-/-}$*Il2rg*$^{-/-}$ mice, 5.5 Gy twice with a 3-hour interval). Neomycin (1 mg/ml) and
671 Polymycin (0.1 mg/ml) were added to the drinking water for 1~2 weeks.

672 For the *Rorc* over-expression experiments, we isolated adult bone marrow progenitors (Lin$^-$c-
673 Kit$^{int/+}$Sca-1$^+$) from wild type (CD45.1) or *Rorc*$^{Gfp/+}$ (CD45.2) mice were transduced them with
674 Rorc-GFP plasmid (*Rorc*^{OE}) or empty plasmid (*Rorc*^{NC}). For *Gata3* over-expression experiment,
675 we transduced progenitors from the fetal liver (Lin$^-$c-Kit$^{int/+}$Sca-1$^+$) with either Gata3-GFP
676 plasmid (*Gata3*^{OE}) or empty plasmid (*Gata3*^{NC}). After Successfully transduction, we sorted and
677 mixed the progenitors with competitor cells (5×10^5 for each recipient mice, total bone marrow
678 from CD45.2 *Rag2*$^{-/-}$*Il2rg*$^{-/-}$ mice) before transferring to the lethally irradiated mice (CD45.1.2
679 wild type, 5.5 Gy twice with a 3-hour interval). Neomycin (1 mg/ml) and Polymycin (0.1 mg/ml)
680 were added to the drinking water for 1~2 weeks. We analyzed cells in the recipient mice 5~6
681 weeks after transfer.

682 **Single-cell RNA-seq library preparation**

683 Single αLP cells were sorted by FACS from embryonic liver (E15.5~16.5) and adult bone
684 marrow. After the confirming of cell purity (above 95%) and the cell viability (above 85%)
685 after sorting, cells were further sent to 10×Genomics sequencing platform for single-cell
686 transcriptome sequencing (Annaroad Gene Technology(Beijing)Co., Ltd).

687 **scRNA-seq data preprocessing and quality control**

688 The transcriptional profiles of individual cells were acquired through a process involving

689 read mapping, removal of background noises, removal of multiplets, and selection of cells
690 of interest. We mapped scRNA-seq reads to the mm10 version *Mus musculus* reference
691 genome from 10x Genomics (https://cf.10xgenomics.com/supp/cell-exp/refdata-gex-
692 mm10-2020-A.tar.gz) using CellRanger v3.1.0 (10x Genomics) 'count' commands. To
693 remove the ambient RNA induced background noises, we removed the used SoupX v1.2.2
694 (Young and Behjati, 2020) to produce clean UMI-droplet matrices. The clean droplets with
695 low UMI counts and high percentages of mitochondrial expressions were removed from
696 the dataset. Besides single cells, the dataset also contained a small fraction of multiplet
697 droplets. We used DoubletFinder v2.0 (McGinnis et al., 2019) to identify these multiplets.
698 After removing multples, the datasets still contained cells we are not interested in because
699 the cell sorting procedure might have false detections. After data normalization and
700 clustering, we removed the clusters with low expression levels of *Ptprc* (non-immune cells
701 mingled in), clusters with high *Cd3e* expressions (T cells mingled in), clusters with high
702 *Cd79a* expressions (B cells mingled in). The feature selection, normalization, scaling,
703 dimensionality reduction, and visualization of data were conducted with the help of single-
704 cell data analyzing suites Seurat v3.2 (Stuart et al., 2019) and Scanpy v1.7 (Wolf et al.,
705 2018).
706 To reveal the identities and intrinsic diffenrentiation potential of the hematopoeitic
707 progenitors, we performed cell mapping analysis to show the affinities between the
708 progenitors and other known cell types. We used SingleR v1.0 (Aran et al., 2019) to map
709 the transcriptional profiles in the ImmGen references to our datasets.
710

711 **scRNA-seq data integratoin**

712 To make cell across different developmental stages and batches comparable, we
713 performed integration analyses using a GPU accelerated implementation of the Harmony
714 algorithm, harmony-pytroch v0.1.7 (https://pypi.org/project/harmony-pytorch) (Korsunsky
715 et al., 2019). The analyses reduced unwanted batch-associated variations and produced
716 harmonized cell latent vectors and under the following parameter settings: theta=5,
717 lambda=0.5.

718 **Cell vector field analysis**

719 The cell state transition streamlines were derived by RNA velocity analyses (La Manno et
720 al., 2018). Velocyto v0.17 was used to convert the bam format read alignment file produced
721 by CellRanger to the unspliced/spliced counts (La Manno et al., 2018). The cell vector field
722 streamlines and the differential geometry analyses were obtained using Dynamo v1.1.0
723 (Qiu et al., 2022).
724 To obtain the representative cells along the velocity trajectories, we calculated the least
725 action path (LAP) along the vector field using the Dynamo package's dyn.pd.least_action()
726 function. The starting and ending states of the LAPs are selected with the help of the
727 Dynamo vector field's fixed points. The outputs of LAP analysis contained *T* UMAP points
728 arranged in the state transition's chronological order. We chose the 10 nearest neighbors
729 in UMAP space for each point and take their average gene expression as a smoothed
730 expression profiles of each point. The cells on the LAP and their neighbors are finally
731 selected as the representative cells along the velocity trajectories. The average gene

732 expressions of each time point creates a representative expression time series (a matrix
733 with *g* rows and *T* columns, *g* is the number of genes in the dataset), which was used for
734 further gene regulatory program analyses.

735 **Gene regulatory module identification**

736 Existing methods for identifying gene regulatory program often suffers from compactness
737 problems, where the identified gene expression events are not concentrated around a
738 specific time point. Here, we proposed the TSC (temporal spatial consensus) algorithm to
739 refine the SCENIC gene regulatory network (GRN) output. TSC algorithm combines the
740 spatial localization information (TF-target genes relationships) and the temporal
741 information (gene expression time series). We used the "grn" and "ctx" command in
742 pySCENIC v0.11 (Van de Sande et al., 2020) to generate a basic GRN backbone.
743 TSC accepted the LAP derived gene expression time series (*g* x *T* matrix) and calculated
744 dynamic time wrapping distances (DTW) between every gene's expression time series
745 (https://zenodo.org/records/7158824). A k-NN (k nearest neighbor) graph was then created
746 using these distances (k=20 by default) and edges on the graph were next dropped out if
747 the two connecting nodes were not mutual k-NN. Given the DTW graph and the SCENIC
748 graph as two layers sharing the same set of nodes (genes), we build a multiplex network.
749 We used Node2Vec (Grover and Leskovec, 2016) for layers of the multiplex network and
750 obtained latent embedding for each genes. A hierarchical clustering from the
751 scipy.cluster.hierarchy package was used to group these genes into different affinity
752 modules, which was the TSC-refined gene regulatory modules.

753 **Differentially Expressed Genes and GSVA analysis**

754 The DEG (differentially expressed genes) were identified with the Seurat package's
755 FindMarkers() or FindAllMarkers() function with an adjusted p-value <0.05 threshold. The
756 DEG analyses compared expressions using Wilcoxon rank sum test on the normalized
757 data slot in Seurat objects.
758 In Gene Set Variation Analysis (GSVA) (Hanzelmann et al., 2013), cells are firstly
759 overclustered within cell types to be analyzed, and the overclustered cells are then merged
760 into metacells by taking their average expression profiles. GSVA analyses were performed
761 on these metacells using gene sets from MSigDB Hallmark (Liberzon et al., 2011).
762 We used the ternary plot (Hamilton and Ferry, 2018) to present the tangled
763 relationships between the *Gata3* regulon, the *Rorc* regulon, and the Notch signaling. The
764 *Gata3* and *Rorc* regulons' gene members were extracted from the SCENIC-derived gene
765 regulatory modules. We used the following Notch signaling pathway gene members:
766 *Notch1*, *Notch2*, *Notch3*, *Notch4*, *Furin*, *Psen2*, *Adam17*, *Dtx1*, *Dtx4*, *Rbpj*. The activation
767 scores of the three modules were evaluated by GSVA. The samples used for GSVA
768 analysis were the average expression profiles of the time steps derived from the LAP
769 analyses.

770 QUANTIFICATION AND STATISTICAL ANALYSIS

771 **Statistical Analysis**

772 GraphPad Prism 7 was used for statistical analysis with the specific tests and the number
773 of samples used for each analysis (n) shown in the figure legends.

774 **REFERENCE**

775 Aran, D., Looney, A.P., Liu, L., Wu, E., Fong, V., Hsu, A., Chak, S., Naikawadi, R.P., Wolters,
776 P.J., Abate, A.R., *et al.* (2019). Reference-based analysis of lung single-cell sequencing reveals
777 a transitional profibrotic macrophage. Nat Immunol *20*, 163-172.
778 Bal, S.M., Golebski, K., and Spits, H. (2020). Plasticity of innate lymphoid cell subsets. Nature
779 reviews Immunology *20*, 552-565.
780 Califano, D., Cho, J.J., Uddin, M.N., Lorentsen, K.J., Yang, Q., Bhandoola, A., Li, H., and Avram,
781 D. (2015). Transcription Factor Bcl11b Controls Identity and Function of Mature Type 2 Innate
782 Lymphoid Cells. Immunity *43*, 354-368.
783 Chea, S., Schmutz, S., Berthault, C., Perchet, T., Petit, M., Burlen-Defranoux, O., Goldrath,
784 A.W., Rodewald, H.R., Cumano, A., and Golub, R. (2016a). Single-Cell Gene Expression
785 Analyses Reveal Heterogeneous Responsiveness of Fetal Innate Lymphoid Progenitors to
786 Notch Signaling. Cell Rep *14*, 1500-1516.
787 Chea, S., Schmutz, S., Berthault, C., Perchet, T., Petit, M., Burlen-Defranoux, O., Goldrath,
788 A.W., Rodewald, H.R., Cumano, A., and Golub, R. (2016b). Single-Cell Gene Expression
789 Analyses Reveal Heterogeneous Responsiveness of Fetal Innate Lymphoid Progenitors to
790 Notch Signaling. Cell Rep *14*, 1500-1516.
791 Cherrier, D.E., Serafini, N., and Di Santo, J.P. (2018). Innate Lymphoid Cell Development: A T
792 Cell Perspective. Immunity *48*, 1091-1103.
793 Cherrier, M., Sawa, S., and Eberl, G. (2012). Notch, Id2, and RORgammat sequentially
794 orchestrate the fetal development of lymphoid tissue inducer cells. J Exp Med *209*, 729-740.
795 Ciofani, M., Knowles, G.C., Wiest, D.L., von Boehmer, H., and Zuniga-Pflucker, J.C. (2006).
796 Stage-specific and differential notch dependency at the alphabeta and gammadelta T lineage
797 bifurcation. Immunity *25*, 105-116.
798 Constantinides, M.G., McDonald, B.D., Verhoef, P.A., and Bendelac, A. (2014). A committed
799 precursor to innate lymphoid cells. Nature *508*, 397-401.
800 De Obaldia, M.E., and Bhandoola, A. (2015). Transcriptional regulation of innate and adaptive
801 lymphocyte lineages. Annual review of immunology *33*, 607-642.
802 Dunon, D., Courtois, D., Vainio, O., Six, A., Chen, C.H., Cooper, M.D., Dangy, J.P., and Imhof,
803 B.A. (1997). Ontogeny of the immune system: gamma/delta and alpha/beta T cells migrate from
804 thymus to the periphery in alternating waves. J Exp Med *186*, 977-988.
805 Eberl, G., Colonna, M., Di Santo, J.P., and McKenzie, A.N. (2015). Innate lymphoid cells. Innate
806 lymphoid cells: a new paradigm in immunology. Science *348*, aaa6566.
807 Eberl, G., Marmon, S., Sunshine, M.J., Rennert, P.D., Choi, Y., and Littman, D.R. (2004). An
808 essential function for the nuclear receptor RORgamma(t) in the generation of fetal lymphoid
809 tissue inducer cells. Nat Immunol *5*, 64-73.
810 Fang, D., and Zhu, J. (2017). Dynamic balance between master transcription factors
811 determines the fates and functions of CD4 T cell and innate lymphoid cell subsets. J Exp Med
812 *214*, 1861-1876.
813 Garbe, A.I., Krueger, A., Gounari, F., Zuniga-Pflucker, J.C., and von Boehmer, H. (2006).
814 Differential synergy of Notch and T cell receptor signaling determines alphabeta versus
815 gammadelta lineage fate. J Exp Med *203*, 1579-1590.
816 Ghaedi, M., Shen, Z.Y., Orangi, M., Martinez-Gonzalez, I., Wei, L., Lu, X., Das, A., Heravi-
817 Moussavi, A., Marra, M.A., Bhandoola, A., *et al.* (2020). Single-cell analysis of RORalpha tracer

818 mouse lung reveals ILC progenitors and effector ILC2 subsets. J Exp Med *217*.
819 Grover, A., and Leskovec, J. (2016). node2vec: Scalable Feature Learning for Networks. KDD
820 *2016*, 855-864.
821 Hamilton, N.E., and Ferry, M. (2018). ggtern: Ternary Diagrams Using ggplot2. Journal of
822 Statistical Software *87*.
823 Hanzelmann, S., Castelo, R., and Guinney, J. (2013). GSVA: gene set variation analysis for
824 microarray and RNA-seq data. BMC Bioinformatics *14*, 7.
825 Harly, C., Kenney, D., Ren, G., Lai, B., Raabe, T., Yang, Q., Cam, M.C., Xue, H.H., Zhao, K.,
826 and Bhandoola, A. (2019). The transcription factor TCF-1 enforces commitment to the innate
827 lymphoid cell lineage. Nat Immunol *20*, 1150-1160.
828 Hepworth, M.R., Monticelli, L.A., Fung, T.C., Ziegler, C.G., Grunberg, S., Sinha, R., Mantegazza,
829 A.R., Ma, H.L., Crawford, A., Angelosanto, J.M.*, et al.* (2013). Innate lymphoid cells regulate
830 CD4+ T-cell responses to intestinal commensal bacteria. Nature *498*, 113-117.
831 Ho, I.C., Tai, T.S., and Pai, S.Y. (2009). GATA3 and the T-cell lineage: essential functions before
832 and after T-helper-2-cell differentiation. Nat Rev Immunol *9*, 125-135.
833 Hoorweg, K., Peters, C.P., Cornelissen, F., Aparicio-Domingo, P., Papazian, N., Kazemier, G.,
834 Mjosberg, J.M., Spits, H., and Cupedo, T. (2012). Functional Differences between Human
835 NKp44(-) and NKp44(+) RORC(+) Innate Lymphoid Cells. Front Immunol *3*, 72.
836 Hosokawa, H., and Rothenberg, E.V. (2021). How transcription factors drive choice of the T cell
837 fate. Nat Rev Immunol *21*, 162-176.
838 Ishizuka, I.E., Chea, S., Gudjonson, H., Constantinides, M.G., Dinner, A.R., Bendelac, A., and
839 Golub, R. (2016). Single-cell analysis defines the divergence between the innate lymphoid cell
840 lineage and lymphoid tissue-inducer cell lineage. Nat Immunol *17*, 269-276.
841 Jassinskaja, M., Johansson, E., Kristiansen, T.A., Akerstrand, H., Sjoholm, K., Hauri, S.,
842 Malmstrom, J., Yuan, J., and Hansson, J. (2017). Comprehensive Proteomic Characterization
843 of Ontogenic Changes in Hematopoietic Stem and Progenitor Cells. Cell Rep *21*, 3285-3297.
844 Jones, R., Cosway, E.J., Willis, C., White, A.J., Jenkinson, W.E., Fehling, H.J., Anderson, G.,
845 and Withers, D.R. (2018). Dynamic changes in intrathymic ILC populations during murine
846 neonatal development. Eur J Immunol *48*, 1481-1491.
847 Kim, I., Saunders, T.L., and Morrison, S.J. (2007). Sox17 dependence distinguishes the
848 transcriptional regulation of fetal from adult hematopoietic stem cells. Cell *130*, 470-483.
849 Kiss, E.A., Vonarbourg, C., Kopfmann, S., Hobeika, E., Finke, D., Esser, C., and Diefenbach,
850 A. (2011). Natural aryl hydrocarbon receptor ligands control organogenesis of intestinal
851 lymphoid follicles. Science *334*, 1561-1565.
852 Klose, C.S.N., Flach, M., Mohle, L., Rogell, L., Hoyler, T., Ebert, K., Fabiunke, C., Pfeifer, D.,
853 Sexl, V., Fonseca-Pereira, D.*, et al.* (2014). Differentiation of type 1 ILCs from a common
854 progenitor to all helper-like innate lymphoid cell lineages. Cell *157*, 340-356.
855 Korsunsky, I., Millard, N., Fan, J., Slowikowski, K., Zhang, F., Wei, K., Baglaenko, Y., Brenner,
856 M., Loh, P.R., and Raychaudhuri, S. (2019). Fast, sensitive and accurate integration of single-
857 cell data with Harmony. Nat Methods *16*, 1289-1296.
858 Krishnamurty, A.T., and Turley, S.J. (2020). Lymph node stromal cells: cartographers of the
859 immune system. Nat Immunol *21*, 369-380.
860 La Manno, G., Soldatov, R., Zeisel, A., Braun, E., Hochgerner, H., Petukhov, V., Lidschreiber,
861 K., Kastriti, M.E., Lonnerberg, P., Furlan, A.*, et al.* (2018). RNA velocity of single cells. Nature

862 *560*, 494-498.
863 Lee, J.S., Cella, M., McDonald, K.G., Garlanda, C., Kennedy, G.D., Nukaya, M., Mantovani, A.,
864 Kopan, R., Bradfield, C.A., Newberry, R.D*., et al.* (2012). AHR drives the development of gut
865 ILC22 cells and postnatal lymphoid tissues via pathways dependent on and independent of
866 Notch. Nat Immunol *13*, 144-151.
867 Li, S., Bostick, J.W., Ye, J., Qiu, J., Zhang, B., Urban, J.F., Jr., Avram, D., and Zhou, L. (2018).
868 Aryl Hydrocarbon Receptor Signaling Cell Intrinsically Inhibits Intestinal Group 2 Innate
869 Lymphoid Cell Function. Immunity *49*, 915-928 e915.
870 Li, S., Heller, J.J., Bostick, J.W., Lee, A., Schjerven, H., Kastner, P., Chan, S., Chen, Z.E., and
871 Zhou, L. (2016). Ikaros Inhibits Group 3 Innate Lymphoid Cell Development and Function by
872 Suppressing the Aryl Hydrocarbon Receptor Pathway. Immunity *45*, 185-197.
873 Liberzon, A., Subramanian, A., Pinchback, R., Thorvaldsdottir, H., Tamayo, P., and Mesirov, J.P.
874 (2011). Molecular signatures database (MSigDB) 3.0. Bioinformatics *27*, 1739-1740.
875 Lim, A.I., and Di Santo, J.P. (2019). ILC-poiesis: Ensuring tissue ILC differentiation at the right
876 place and time. Eur J Immunol *49*, 11-18.
877 Lim, A.I., Li, Y., Lopez-Lastra, S., Stadhouders, R., Paul, F., Casrouge, A., Serafini, N., Puel, A.,
878 Bustamante, J., Surace, L*., et al.* (2017). Systemic Human ILC Precursors Provide a Substrate
879 for Tissue ILC Differentiation. Cell *168*, 1086-1100 e1010.
880 Lyu, M., Suzuki, H., Kang, L., Gaspal, F., Zhou, W., Goc, J., Zhou, L., Zhou, J., Zhang, W., Bank,
881 J.R.I.L.C*., et al.* (2022). ILC3s select microbiota-specific regulatory T cells to establish tolerance
882 in the gut. Nature *610*, 744-751.
883 Mao, K., Baptista, A.P., Tamoutounour, S., Zhuang, L., Bouladoux, N., Martins, A.J., Huang, Y.,
884 Gerner, M.Y., Belkaid, Y., and Germain, R.N. (2018). Innate and adaptive lymphocytes
885 sequentially shape the gut microbiota and lipid metabolism. Nature *554*, 255-259.
886 McGinnis, C.S., Murrow, L.M., and Gartner, Z.J. (2019). DoubletFinder: Doublet Detection in
887 Single-Cell RNA Sequencing Data Using Artificial Nearest Neighbors. Cell Syst *8*, 329-337
888 e324.
889 Medvinsky, A., Rybtsov, S., and Taoudi, S. (2011). Embryonic origin of the adult hematopoietic
890 system: advances and questions. Development *138*, 1017-1031.
891 Mielke, L.A., Groom, J.R., Rankin, L.C., Seillet, C., Masson, F., Putoczki, T., and Belz, G.T.
892 (2013). TCF-1 controls ILC2 and NKp46+RORgammat+ innate lymphocyte differentiation and
893 protection in intestinal inflammation. J Immunol *191*, 4383-4391.
894 Oherle, K., Acker, E., Bonfield, M., Wang, T., Gray, J., Lang, I., Bridges, J., Lewkowich, I., Xu,
895 Y., Ahlfeld, S*., et al.* (2020). Insulin-like Growth Factor 1 Supports a Pulmonary Niche that
896 Promotes Type 3 Innate Lymphoid Cell Development in Newborn Lungs. Immunity *52*, 275-294
897 e279.
898 Onder, L., and Ludewig, B. (2018). A Fresh View on Lymph Node Organogenesis. Trends
899 Immunol *39*, 775-787.
900 Possot, C., Schmutz, S., Chea, S., Boucontet, L., Louise, A., Cumano, A., and Golub, R. (2011).
901 Notch signaling is necessary for adult, but not fetal, development of RORgammat(+) innate
902 lymphoid cells. Nat Immunol *12*, 949-958.
903 Qiu, X., Zhang, Y., Martin-Rufino, J.D., Weng, C., Hosseinzadeh, S., Yang, D., Pogson, A.N.,
904 Hein, M.Y., Hoi Joseph Min, K., Wang, L*., et al.* (2022). Mapping transcriptomic vector fields of
905 single cells. Cell *185*, 690-711 e645.

906 Ren, G., Lai, B., Harly, C., Baek, S., Ding, Y., Zheng, M., Cao, Y., Cui, K., Yang, Y., Zhu, J.*, et*
907 *al.* (2022). Transcription factors TCF-1 and GATA3 are key factors for the epigenetic priming of
908 early innate lymphoid progenitors toward distinct cell fates. Immunity *55*, 1402-1413 e1404.
909 Rothenberg, E.V. (2019). Programming for T-lymphocyte fates: modularity and mechanisms.
910 Genes Dev *33*, 1117-1135.
911 Sanos, S.L., Bui, V.L., Mortha, A., Oberle, K., Heners, C., Johner, C., and Diefenbach, A. (2009).
912 RORgammat and commensal microflora are required for the differentiation of mucosal
913 interleukin 22-producing NKp46+ cells. Nat Immunol *10*, 83-91.
914 Sawa, S., Cherrier, M., Lochner, M., Satoh-Takayama, N., Fehling, H.J., Langa, F., Di Santo,
915 J.P., and Eberl, G. (2010). Lineage relationship analysis of RORgammat+ innate lymphoid cells.
916 Science *330*, 665-669.
917 Schjerven, H. (2013). Selective regulation of lymphopoiesis and leukemogenesis by individual
918 zinc fingers of Ikaros. Nat Immunol *4*, 1073-1085.
919 Stuart, T., Butler, A., Hoffman, P., Hafemeister, C., Papalexi, E., Mauck, W.M., 3rd, Hao, Y.,
920 Stoeckius, M., Smibert, P., and Satija, R. (2019). Comprehensive Integration of Single-Cell Data.
921 Cell *177*, 1888-1902 e1821.
922 Tanigaki, K., Tsuji, M., Yamamoto, N., Han, H., Tsukada, J., Inoue, H., Kubo, M., and Honjo, T.
923 (2004). Regulation of alphabeta/gammadelta T cell lineage commitment and peripheral T cell
924 responses by Notch/RBP-J signaling. Immunity *20*, 611-622.
925 Van de Sande, B., Flerin, C., Davie, K., De Waegeneer, M., Hulselmans, G., Aibar, S., Seurinck,
926 R., Saelens, W., Cannoodt, R., Rouchon, Q.*, et al.* (2020). A scalable SCENIC workflow for
927 single-cell gene regulatory network analysis. Nat Protoc *15*, 2247-2276.
928 Vivier, E., Artis, D., Colonna, M., Diefenbach, A., Di Santo, J.P., Eberl, G., Koyasu, S., Locksley,
929 R.M., McKenzie, A.N.J., Mebius, R.E.*, et al.* (2018). Innate Lymphoid Cells: 10 Years On. Cell
930 *174*, 1054-1066.
931 Vonarbourg, C., Mortha, A., Bui, V.L., Hernandez, P.P., Kiss, E.A., Hoyler, T., Flach, M.,
932 Bengsch, B., Thimme, R., Holscher, C.*, et al.* (2010). Regulated expression of nuclear receptor
933 RORgammat confers distinct functional fates to NK cell receptor-expressing RORgammat(+)
934 innate lymphocytes. Immunity *33*, 736-751.
935 Walker, J.A., Barlow, J.L., and McKenzie, A.N. (2013). Innate lymphoid cells--how did we miss
936 them? Nature reviews Immunology *13*, 75-87.
937 Wolf, F.A., Angerer, P., and Theis, F.J. (2018). SCANPY: large-scale single-cell gene expression
938 data analysis. Genome Biol *19*, 15.
939 Wong, S.H., Walker, J.A., Jolin, H.E., Drynan, L.F., Hams, E., Camelo, A., Barlow, J.L., Neill,
940 D.R., Panova, V., Koch, U.*, et al.* (2012). Transcription factor RORalpha is critical for nuocyte
941 development. Nat Immunol *13*, 229-236.
942 Yagi, R., Zhong, C., Northrup, D.L., Yu, F., Bouladoux, N., Spencer, S., Hu, G., Barron, L.,
943 Sharma, S., Nakayama, T.*, et al.* (2014). The transcription factor GATA3 is critical for the
944 development of all IL-7Ralpha-expressing innate lymphoid cells. Immunity *40*, 378-388.
945 Yang, Q., Li, F., Harly, C., Xing, S., Ye, L., Xia, X., Wang, H., Wang, X., Yu, S., Zhou, X.*, et al.*
946 (2015). TCF-1 upregulation identifies early innate lymphoid progenitors in the bone marrow.
947 Nat Immunol *16*, 1044-1050.
948 Young, M.D., and Behjati, S. (2020). SoupX removes ambient RNA contamination from droplet-
949 based single-cell RNA sequencing data. Gigascience *9*.

Yu, Y., Tsang, J.C.H., Wang, C., Clare, S., Wang, J., Chen, X., Brandt, C., Kane, L., Campos, L.S., Lu, L.*, et al.* (2016). Single-cell RNA-seq identifies a PD-1hi ILC progenitor and defines its development pathway. Nature *539*, 102-106.

Yuan, J., Nguyen, C.K., Liu, X., Kanellopoulou, C., and Muljo, S.A. (2012). Lin28b reprograms adult bone marrow hematopoietic progenitors to mediate fetal-like lymphopoiesis. Science *335*, 1195-1200.

Zeis, P., Lian, M., Fan, X., Herman, J.S., Hernandez, D.C., Gentek, R., Elias, S., Symowski, C., Knopper, K., Peltokangas, N.*, et al.* (2020). In Situ Maturation and Tissue Adaptation of Type 2 Innate Lymphoid Cell Progenitors. Immunity *53*, 775-792 e779.

Zhong, C., Cui, K., Wilhelm, C., Hu, G., Mao, K., Belkaid, Y., Zhao, K., and Zhu, J. (2015). Group 3 innate lymphoid cells continuously require the transcription factor GATA-3 after commitment. Nature Immunology.

Zhong, C., Cui, K., Wilhelm, C., Hu, G., Mao, K., Belkaid, Y., Zhao, K., and Zhu, J. (2016). Group 3 innate lymphoid cells continuously require the transcription factor GATA-3 after commitment. Nat Immunol *17*, 169-178.

Zhong, C., Zheng, M., Cui, K., Martins, A.J., Hu, G., Li, D., Tessarollo, L., Kozlov, S., Keller, J.R., Tsang, J.S.*, et al.* (2020). Differential Expression of the Transcription Factor GATA3 Specifies Lineage and Functions of Innate Lymphoid Cells. Immunity *52*, 83-95 e84.

Figures

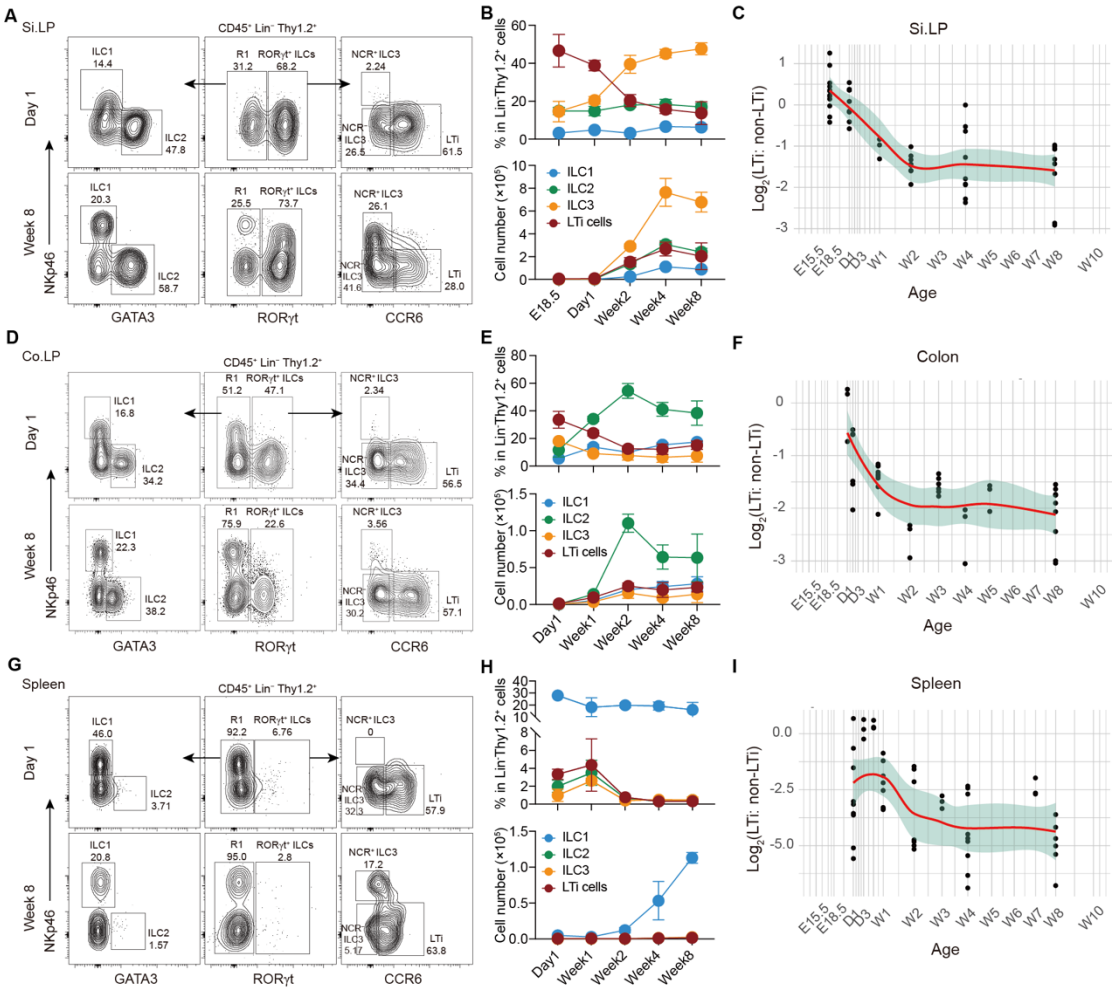

Figure 1 Temporal and tissue distribution of innate lymphoid cells during ontogeny

(A, D and G) Representative FACS plots show the frequencies of major ILC subsets in (A) lamina propria of small intestine (Si.LP), (D) lamina propria of colon (Co.LP) and (G) spleen, between newborn (Day 1) and adult (Week 8) mice.

(B, E and H) The percentage and absolute number of ILC subsets in (B) Si.LP, (E) Co.LP and (H) spleen during ontogeny are shown. Data (n=3-6 mice per group) represent two independent experiments (mean ± SD).

(C, F, I) The logarithm of the percentage ratio of LTi cells to non-LTi ILCs in (C) Si.LP, (F) Co.LP, and (I) spleen are plotted. Each dot represents the value for one individual mouse.

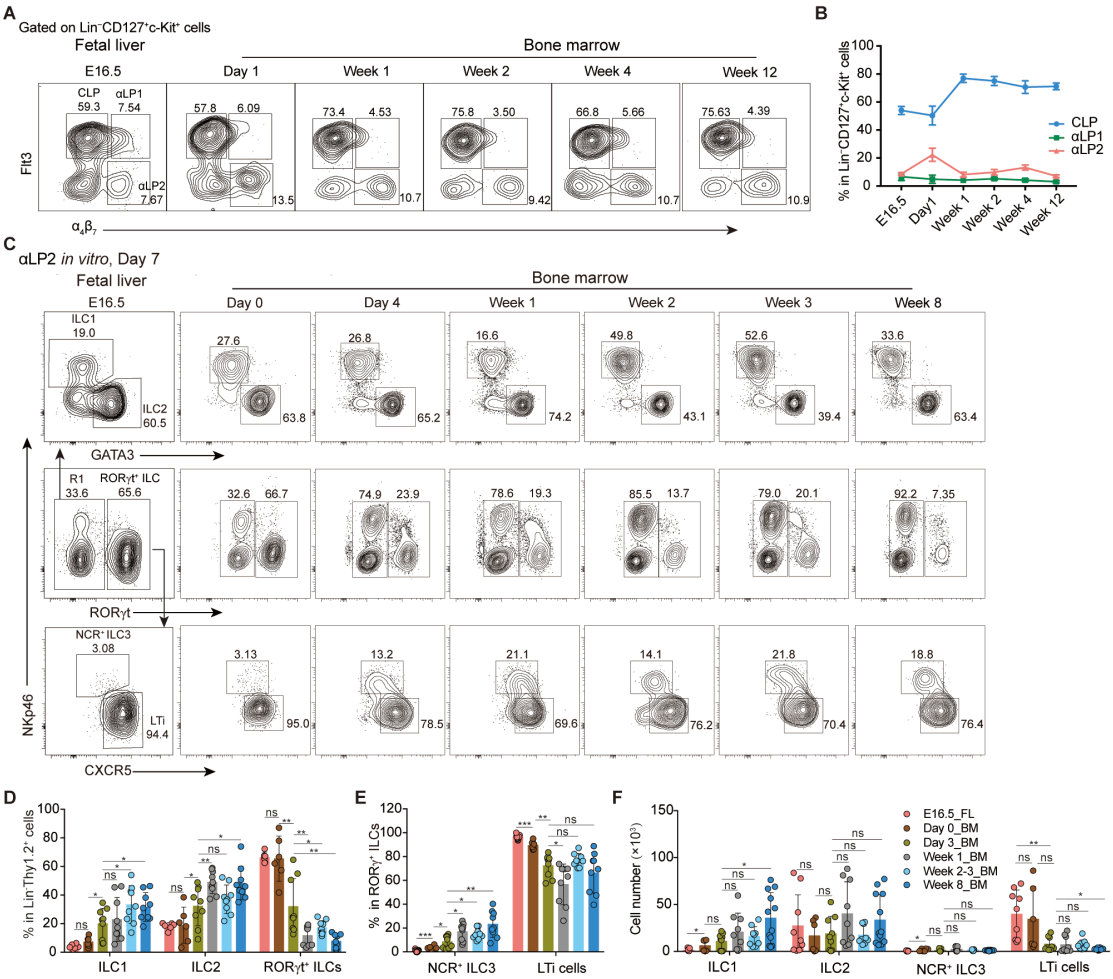

Figure 2 ILC subsets generated by progenitors from different stages during ontogeny

(A) CD45⁺Lin⁻CD127⁺c-Kit$^{int/+}$ cells were gated to identify CLP, αLP1, and αLP2 in fetal liver (E16.5) and bone marrow at neonatal (Day 1), infant (Day 4, Week 1, and Week 2), weaning (Week 4), and adult stages (Week 12).

(B) Dynamic percentages of CLPs, αLP1s, and αLP2s during ontogeny. Data (n=10 mice per group) are pooled from two independent experiments (mean ± SD).

(C) Representative FACS plots show ILC subsets derived from αLP2s sorted from fetal liver (E16.5), or bone marrow at the newborn (Day 0), infant (Day 4 and Week 1), weaning (Week 2-3) and adult mice (Week 8), after 7 days of *in vitro* culture with IL-7 and SCF.

(D-F) Percentage (D-E) and absolute cell number (F) of major ILC subsets in (C). Data (n=6-15 per group) are pooled from three independent experiments (mean ± SD).

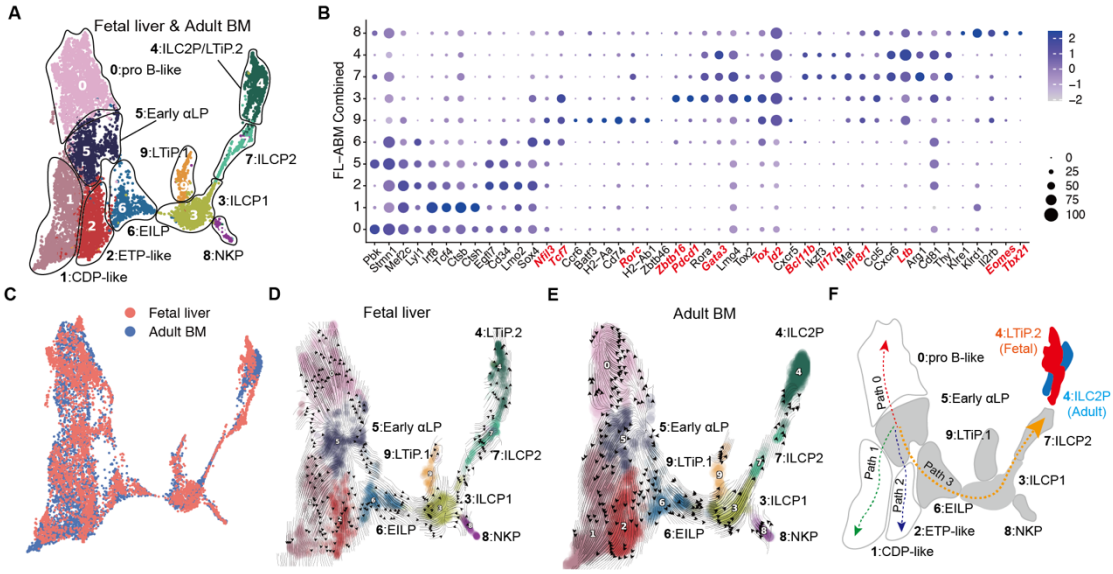

Figure 3 ILC differentiation trajectories in fetal liver and adult bone marrow revealed by single-cell RNA-sequencing analysis.

(A) The cellular composition of αLPs from integrated fetal liver and adult bone marrow is visualized using Uniform Manifold Approximation and Projection (UMAP). Cell types are color-coded.

(B) Feature gene expression is shown across the identified clusters among αLPs using dot-plot analyses.

(C) The integrated UMAP shows αLPs from fetal liver (red) and adult bone marrow (blue).

(D and E) RNA velocity algorithm-derived transition probabilities projected onto UMAP plots of (D) fetal liver and (E) adult bone marrow αLPs. Streamlines represent averaged and projected RNA velocities.

(F) Schematic diagram showing the potential ILC differentiation trajectories in fetal liver and adult bone marrow.

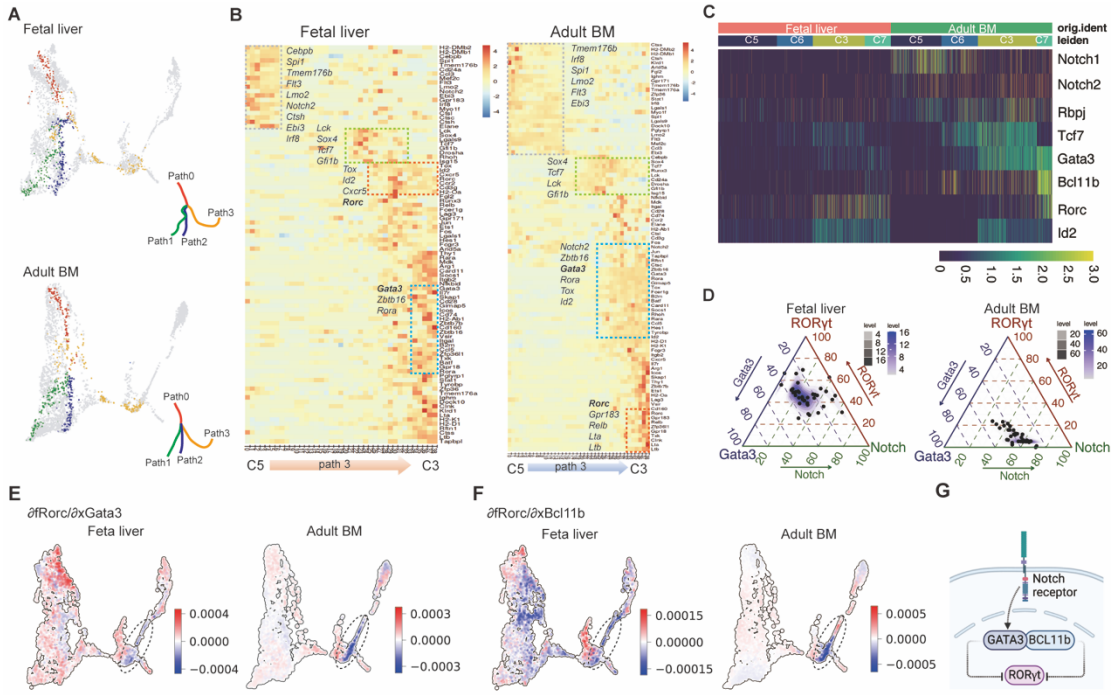

Figure 4 Comparation of gene programs during fetal and adult ILC development

(A) Visualization of the representative cells along the paths revealed in fetal liver and adult bone marrow αLPs.

(B) Heatmaps displaying differentially expressed genes along the ILC differentiation pseudotime (path 3) from early αLP1s (C5) to ILCPs (C3) in fetal liver and adult bone marrow.

(C) Heatmap of gene expressions associated with Notch signaling, *Gata3*, *Bcl11b*, and *Rorc* during both fetal and adult ILC differentiation.

(D) Ternay plots showing mutual relationships among activation scores of Notch signaling pathway, GATA3 regulon, RORγt regulon. The activation scores were evaluated along the ILC differentiation trajectories (Path 3) in fetal and adult stages. Colors of the dashed lines indicate the projection direction of the coordinates.

(E and F) *Dynamo* analysis predicting the potential relationship between (E) *Rorc* and *Gata3*, as well as between (F) *Rorc* and *Bcl11b* during fetal and adult ILC development trajectories. The dashed circles highlighted the negative regulatory relationships revealed by negative Jacobian values.

(G) Schematic diagram showing the potential relationship among Notch signaling, GATA3/BCL11b and RORγt.

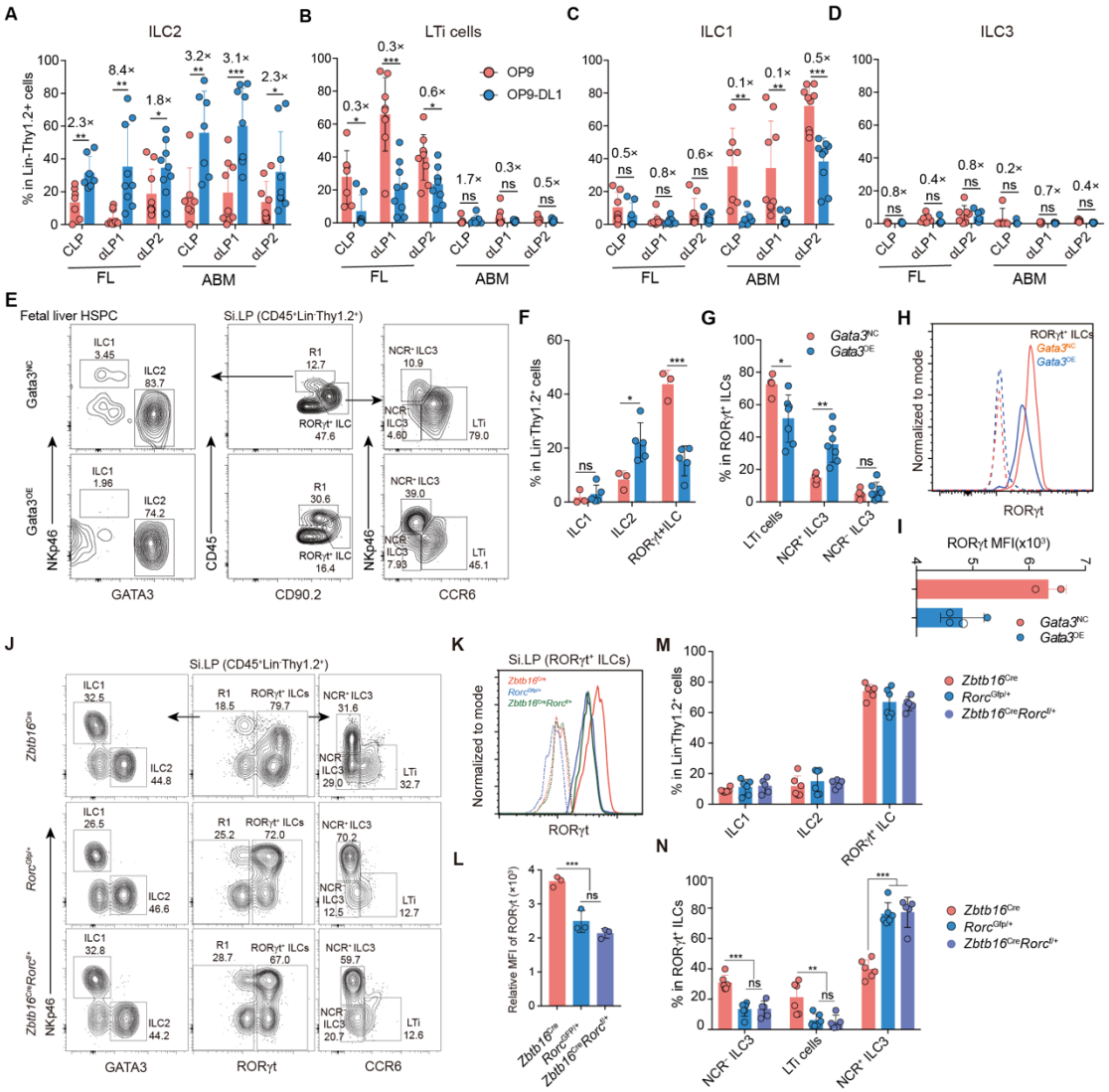

Figure 5 Enhanced Notch signaling, increased GATA3 and decreased RORγt suppresses LTi cell differentiation.

(A-D) Percentage of ILC1s, ILC2s, ILC3 and LTi cells derived from fetal and adult CLPs, αLP1s and αLP2s after co-culture with either OP9 or OP9-DL1 stromal cells *in vitro*. Data (n=7-8 mice per group) are pooled from three to four independent experiments (mean ± SD).

(E) Representative flow cytometry plots showing the ILC subsets derived *in vivo* from the fetal liver progenitors transduced with either empty plasmid (*Gata3*^{NC}) or *Gata3* overexpression (*Gata3*^{OE}) in the recipient intestine.

(F-G) The percentage of ILC subsets in (E). Data (n=3-7 mice per group) are pooled from two independent experiments (mean ± SD).

(H and I) Intracellular staining of RORγt in RORγt^{+} ILCs in (G). Data (n= 2-3 mice per group) represent two independent experiments (mean ± SD).

(J) Flow cytometry analysis showing the major ILC subsets in the small intestine of *Rorc* heterozygous mice, including both *Rorc*$^{Gfp/+}$ and *Zbtb16*^{Cre}*Rorc*$^{f/+}$ mice.

(K and L) Mean fluorescence intensity (MFI) of RORγt in small intestinal RORγt^{+} ILCs from *Rorc* heterozygous mice. Data (n=3 per group) represent two independent experiments

(mean ± SD).

(M and N) Percentage of major ILC subsets in the small intestine from *Rorc* heterozygous mice. Data (n=3 per group) represent two independent experiments (mean ± SD).

Supplementary figures

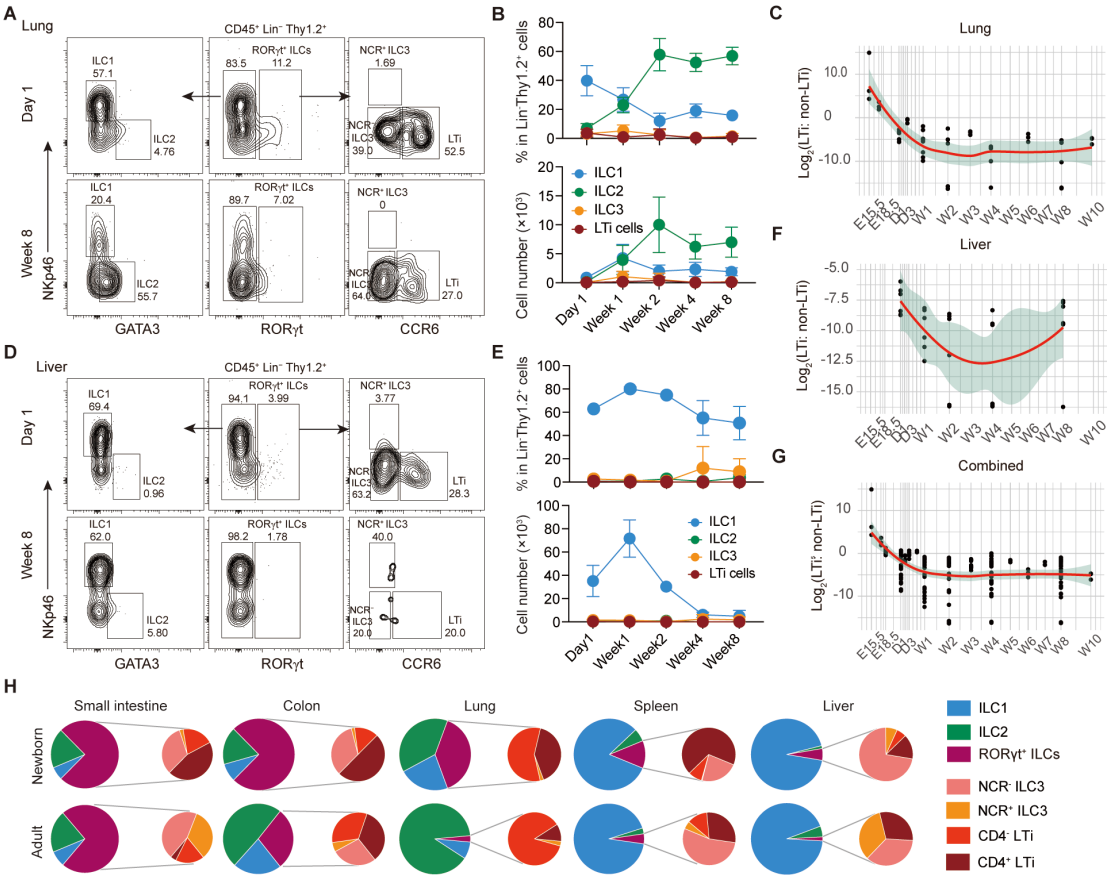

Figure S1 ILC Subsets in lung and liver during ontogeny. Related to Figure 1.

（A and D) Representative FACS plots display the frequencies of major ILC subsets in (A) lung and (D) liver of the newborn (Day 1) and adult (Week 8) mice.

(B and E) Percentage and absolute number of ILC subsets in (B) lung and (E) liver during ontogeny are presented. Data (n=3 mice for each group) represent two independent experiments and are shown as mean ± SD.

(C, F and G) The logarithm of the percentage ratio of LTi cells to non-LTi ILCs in (H) liver, (I) lung, and (G) all these tissues combined. Each dot represents the value for one individual mouse.

(H) A pie graph is provided to illustrate the composition of ILC subsets across tissues between the newborn (Day 1) and adult (Week 8).

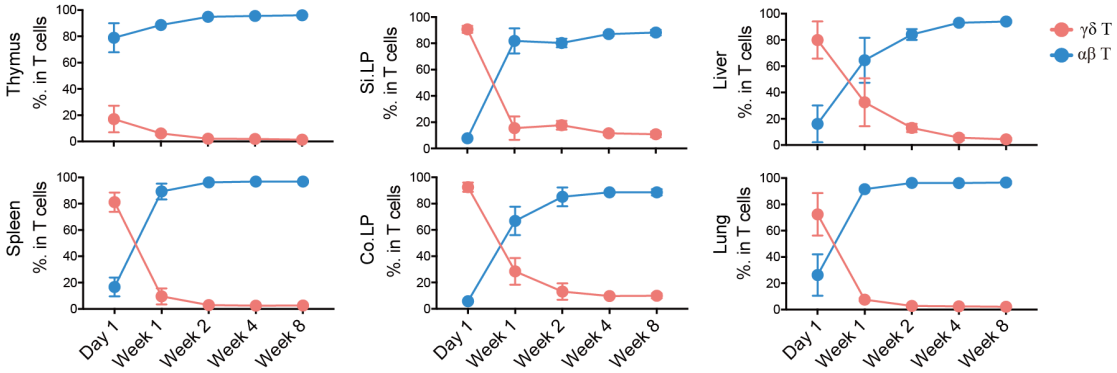

Figure S2 Ontogeny of αβ T cells and γδ T cells. Related to Figure 1.

The percentage of the αβ T cells and γδ T cells in indicated tissues during ontogeny. Data (n= 6 mice per group) are pooled from two independent experiments (mean ± SD).

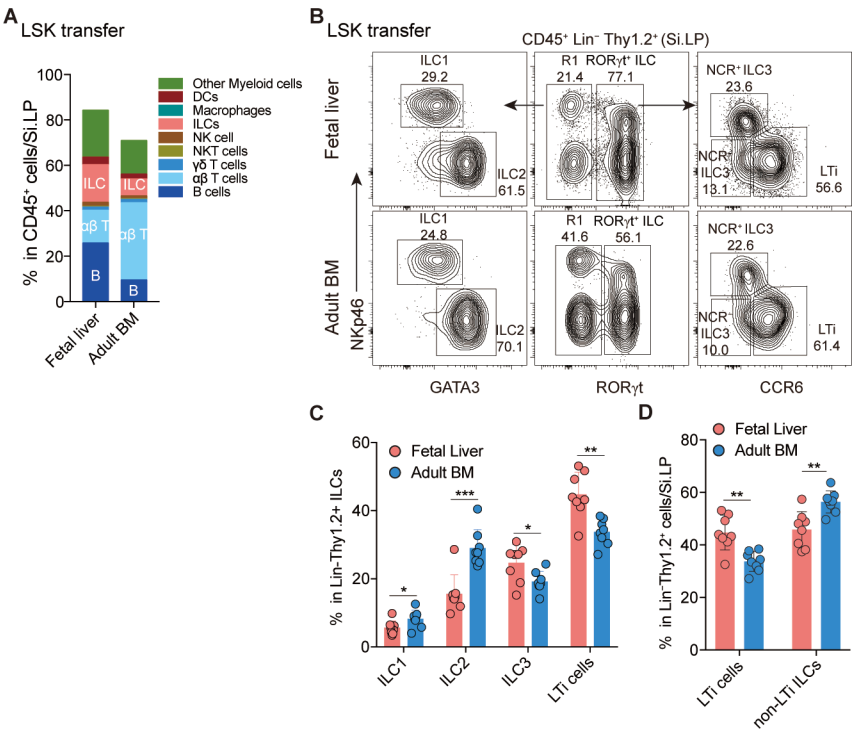

Figure S3 ILC subsets generated by fetal and adult hematopoietic progenitors. Related to Figure 2.

(A) Composition of major immune cells derived from LSKs of fetal liver and adult bone marrow in the recipient small intestine. Data (n=8 mice pre group) are pooled from three independent experiments.

(B) Representative FACS plots show the major ILC subsets derived from LSKs of fetal liver and adult bone marrow in the recipient small intestine.

(C) Percentage of major ILC subsets derived from fetal and adult LSKs in the recipient small intestine.

(D) Proportion of LTi cells and non-LTi ILCs derived from LSKs of fetal liver and adult bone marrow in the recipient small intestine. Data (n= 8 mice per group) are pooled from three independent experiments.

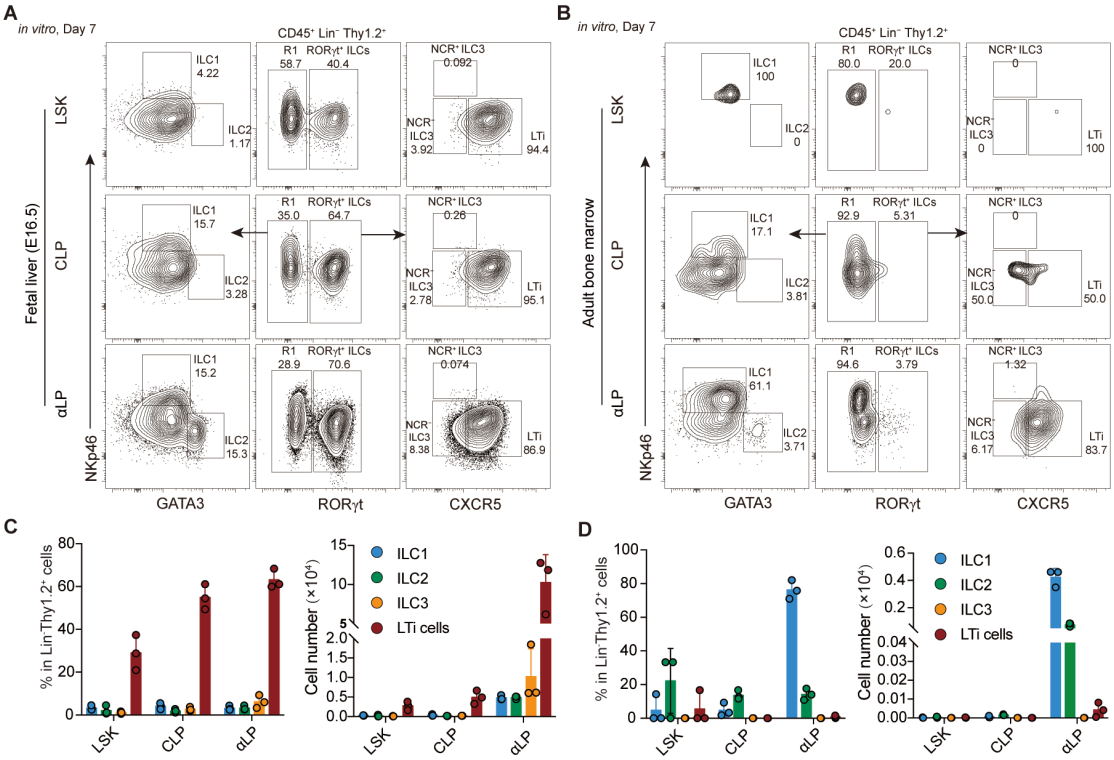

Figure S4 Differentiation assay of ILC progenitors from fetal liver and adult bone marrow. Related to Figure 2.

(A-B) Representative FACS plots display the ILC subsets derived from (A) fetal liver and (B) adult bone marrow LSKs, CLPs and αLPs, after seven days of culture supplemented with IL-7 and SCF *in vitro*.

(C-D) The composition of major ILC subsets among the daughter cells derived from the indicated counterpart progenitors from (C) fetal liver and (D) adult bone marrow are presented. Data (n=3 samples per group) represent two independent experiments and are shown as mean ± SD.

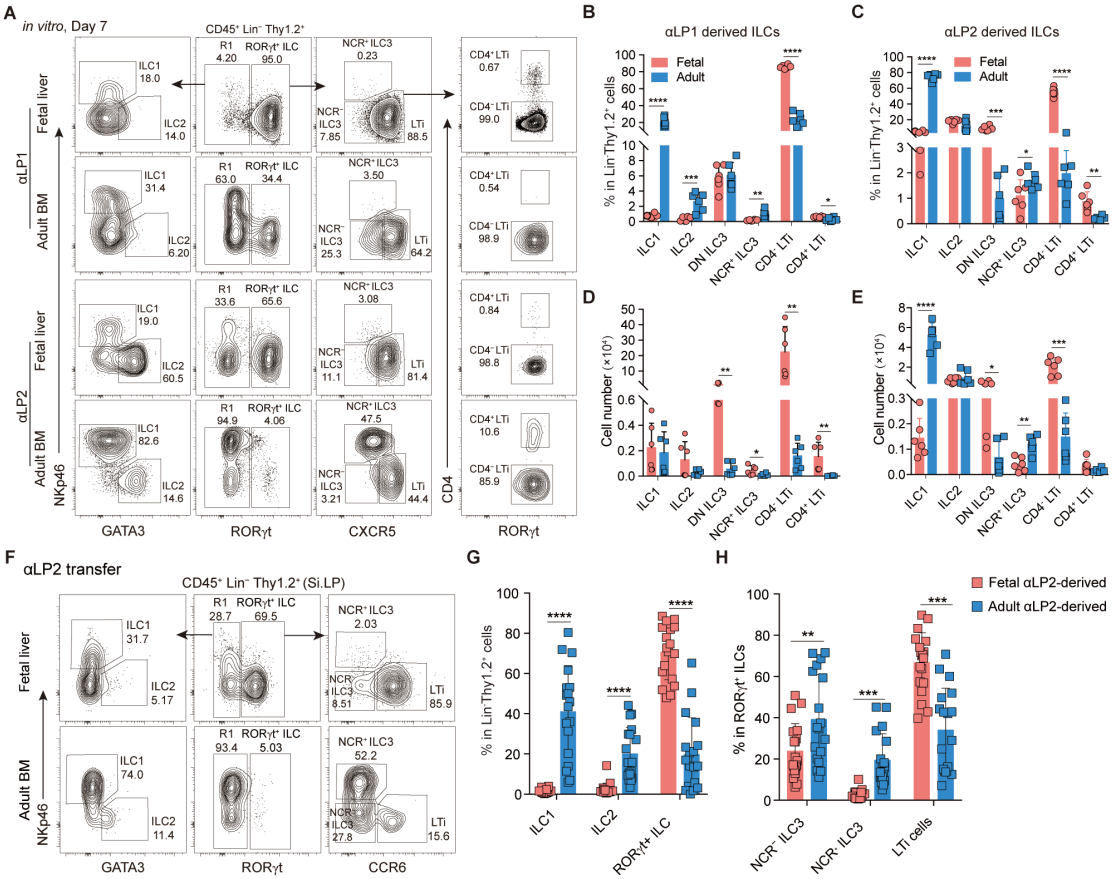

Figure S5 Differentiation assay of αLP1s and αLP2s from fetal liver and adult bone marrow. Related to Figure 2.

(A) Representative FACS plots display the ILC subsets derived from fetal and adult αLP1s or αLP2s after seven days of culture with IL-7 and SCF *in vitro*.

(B-E) The (B-C) percentage and (D-E) absolute number of major ILC subsets derived from fetal and adult (B, D) αLP1s or (C, E) αLP2s are presented. Data (n=6 samples per group) are pooled from two independent experiments and are shown as mean ± SD.

(F) Representative FACS plots show ILC subsets derived from fetal and adult αLP2s in the small intestine of recipient mice.

(G-H) Percentage of (G) ILC1, ILC2 and RORγt$^+$ ILCs and (H) RORγt$^+$ ILC subsets derived from fetal and adult αLP2s in the recipient small intestine. Data (n=18 samples per group) are pooled from seven independent experiments (mean ± SD).

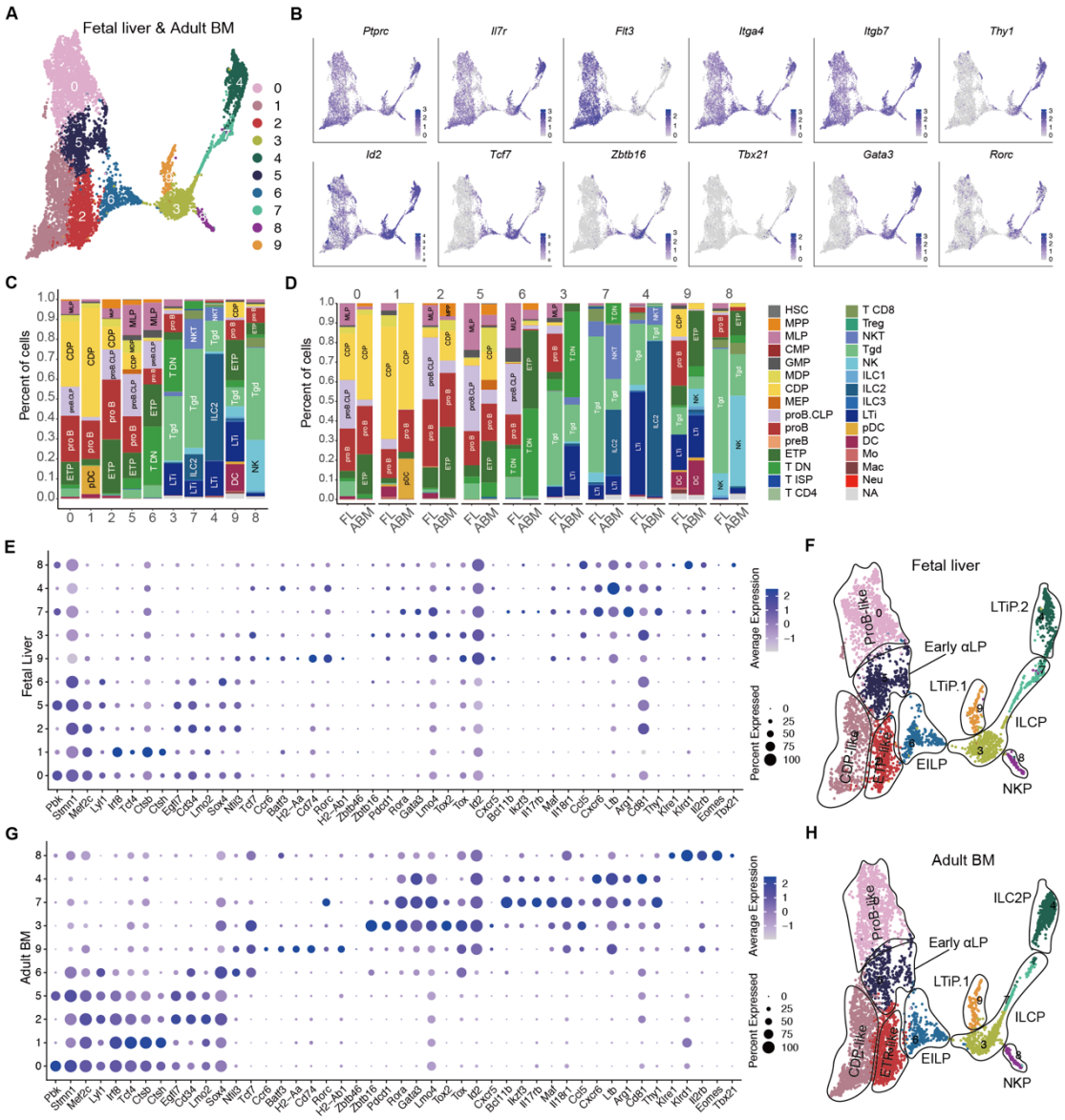

Figure S6 Single-cell transcriptomic landscape of fetal and adult ILC progenitors. Related to Figure 3.

(A) The cellular composition of αLPs from integrated fetal liver and adult bone marrow is visualized using Uniform Manifold Approximation and Projection (UMAP). Cell types are color-coded.

(B) Marker gene expression is shown across the identified clusters among αLPs by feature-plot analysis.

(C and D) Histograms show the top correlated cell types in each (C) integrated or (D) separated cluster by comparing the single-cell transcriptome to that in the ImmGen database.

(E and G) Dot-plot representations of the marker gene expression for the identified clusters among αLPs from (E) fetal liver and (G) adult bone marrow are presented.

(F and H) The indicated clusters in (F) fetal liver and (H) adult bone marrow αLPs are finely annotated.

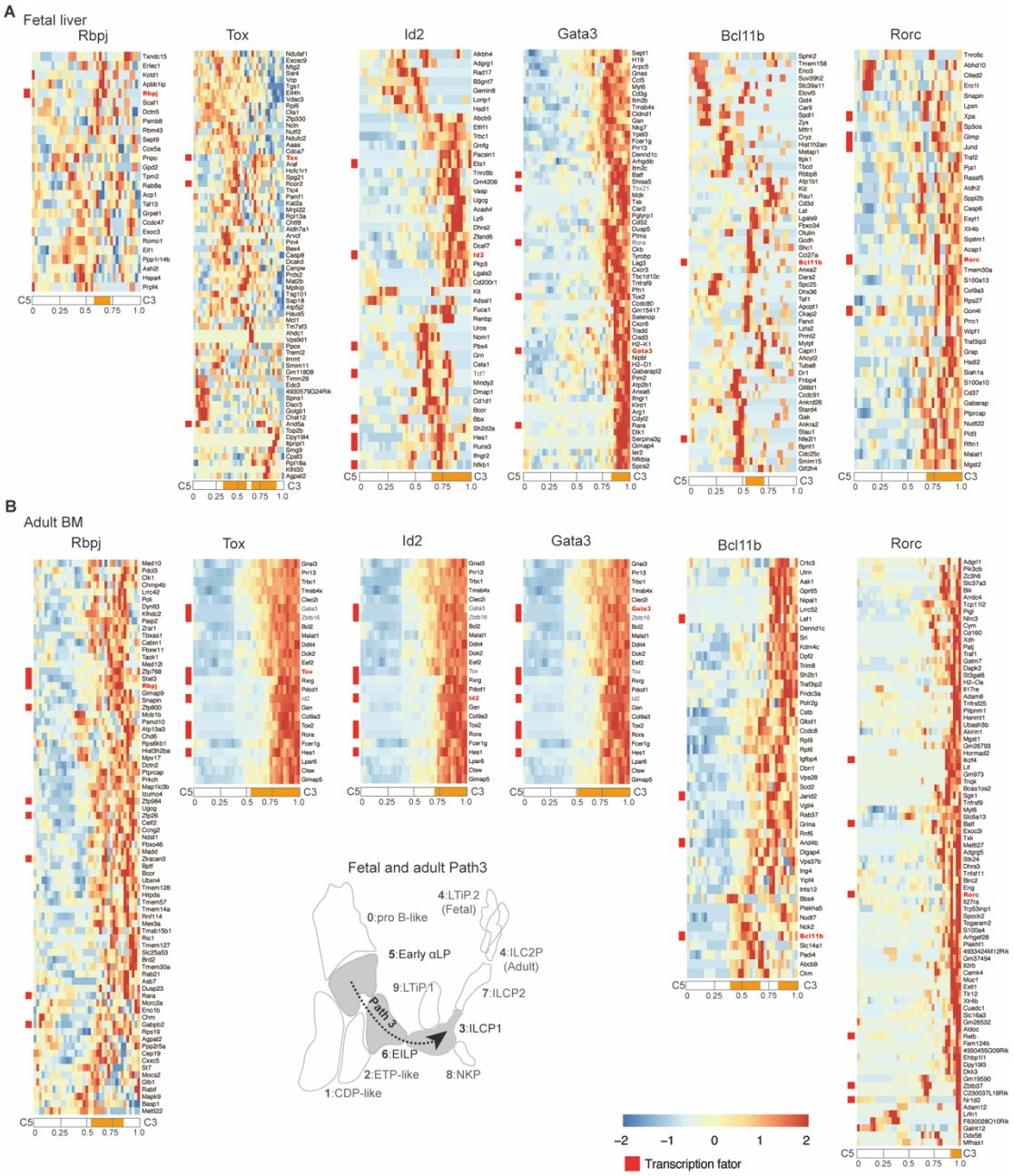

Figure S7 TSC analysis of indicated transcription factors during fetal and adult ILC development revealed by single-cell RNA-sequence. Related to Figure 4.

(A and B) Heatmap showing the expression of genes accompanied with indicated transcription factors along the ILC differentiation pseudotime (path 3) predicted by TSC analysis in (A) fetal liver and (B) adult bone marrow. The red characters mark the transcription factors. The pseudotime from C5 to C3 (path 3) is divided into four equal parts. The orange characters bend during the pseudotime, representing the expression period of the indicated transcription factor.

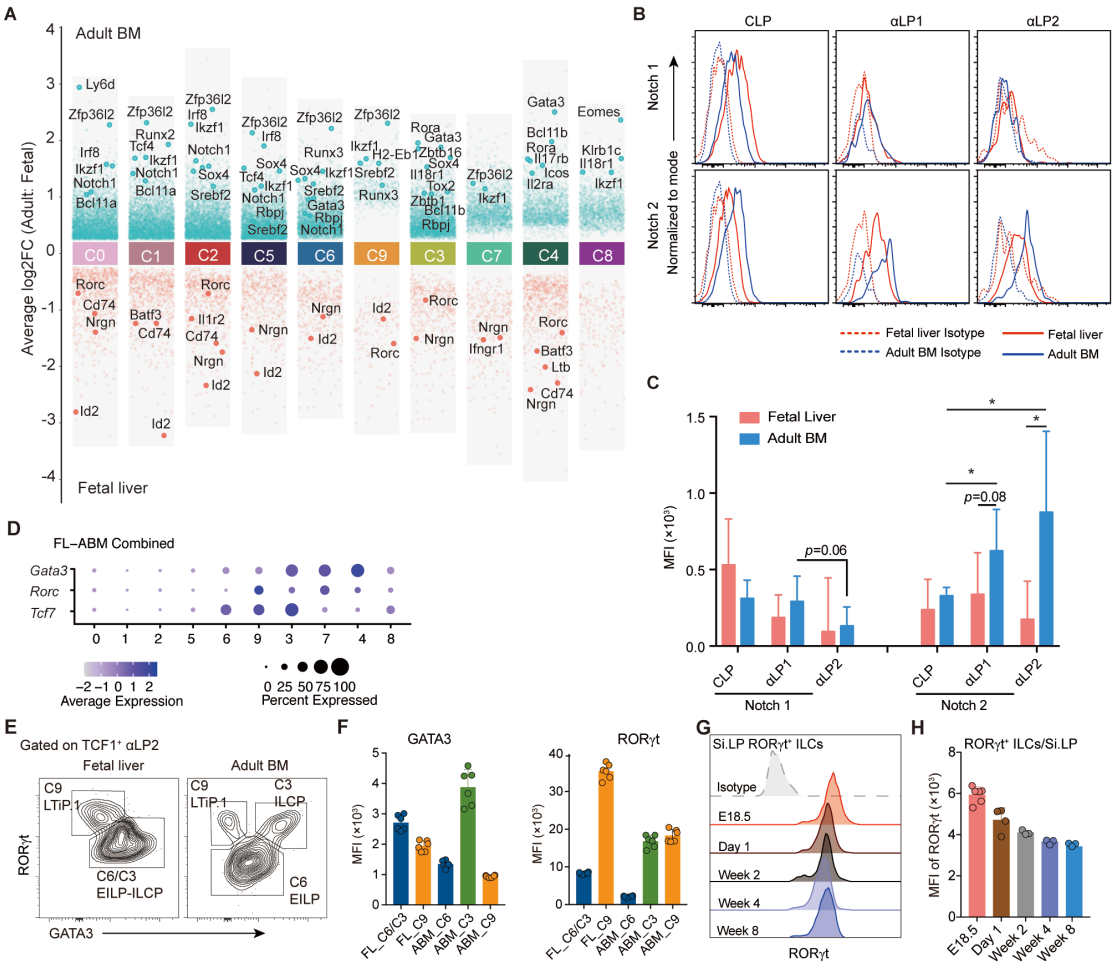

Figure S8 Different expression of genes involved in Notch signaling, *Gata3* and *Rorc* between fetal and adult. Related to Figure 4.

(A) Differentially expressed genes between indicated clusters in fetal liver and adult bone marrow.

(B and C) Flow cytometry analysis showing the expression of Notch1 and Notch2 on ILC progenitors, including CLPs, αLP1s and αLP2s, from both fetal liver and adult bone marrow. Data (n=6-7 samples per group) are pooled from three independent experiments and are presented as mean ± SD.

(D) Dot plots showing expression features of *Tcf7*, *Gata3*, and *Rorc* in ILC progenitors.

(E-F) Flow cytometry analysis showing expression of RORγt and GATA3 in fetal and adult TCF1⁺ αLP2s. Data (n=6 per group) represent two independent experiments (mean ± SD).

(G) Flow cytometry plots showing the intracellular expression level of RORγt in intestinal RORγt⁺ ILCs at different stages.

(H) Mean fluorescence intensity (MFI) of RORγt in small intestinal RORγt⁺ ILCs during ontogeny. Data (n=3-6 per group) are pooled from two independent experiments and shown as mean ± SD.

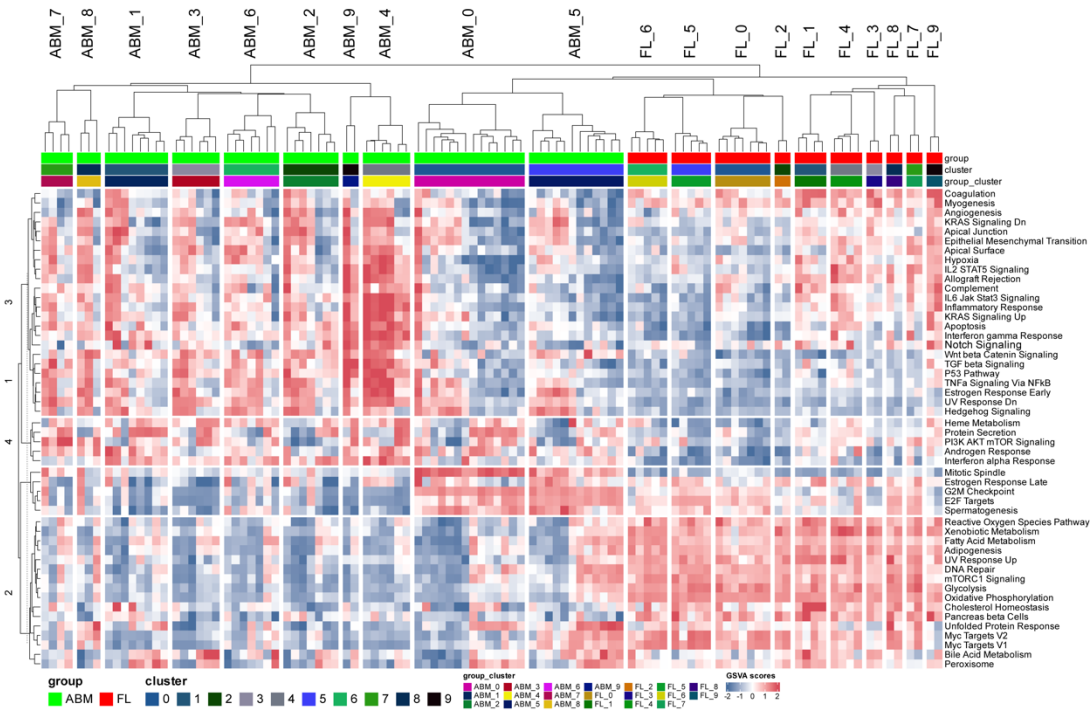

Figure S9 Differentially distributed signaling pathways between fetal and adult αLPs. Related to Figure 4.

Gene signature analyses and clustering of gene set variation analysis (GSVA) scores for single αLPs from fetal liver (Right) and adult bone marrow (Left).

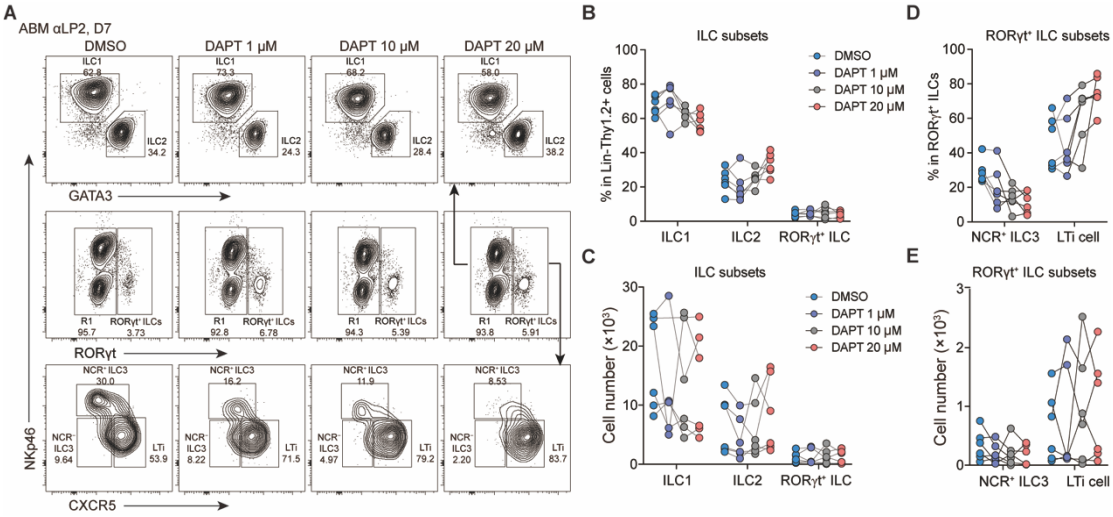

Figure S10 Blocking Notch signaling led to increased LTi cells but decreased NCR⁺ ILC3s generation by adult αLP2s. Related to Figure 5.

(A) Notch signaling inhibitor DAPT was administered during the *in vitro* differentiation of adult bone marrow αLP2s with varying concentrations. Representative flow cytometry plots showing the major ILC subsets among the daughter cells.

(B-C) Percentage (B) and cell number (C) of ILC1s, ILC2s, and RORγt⁺ ILCs in (A).

(D-E) Percentage (D) and cell number (E) in (A). Data (n=6 per group) represent three independent experiments (mean ± SD).

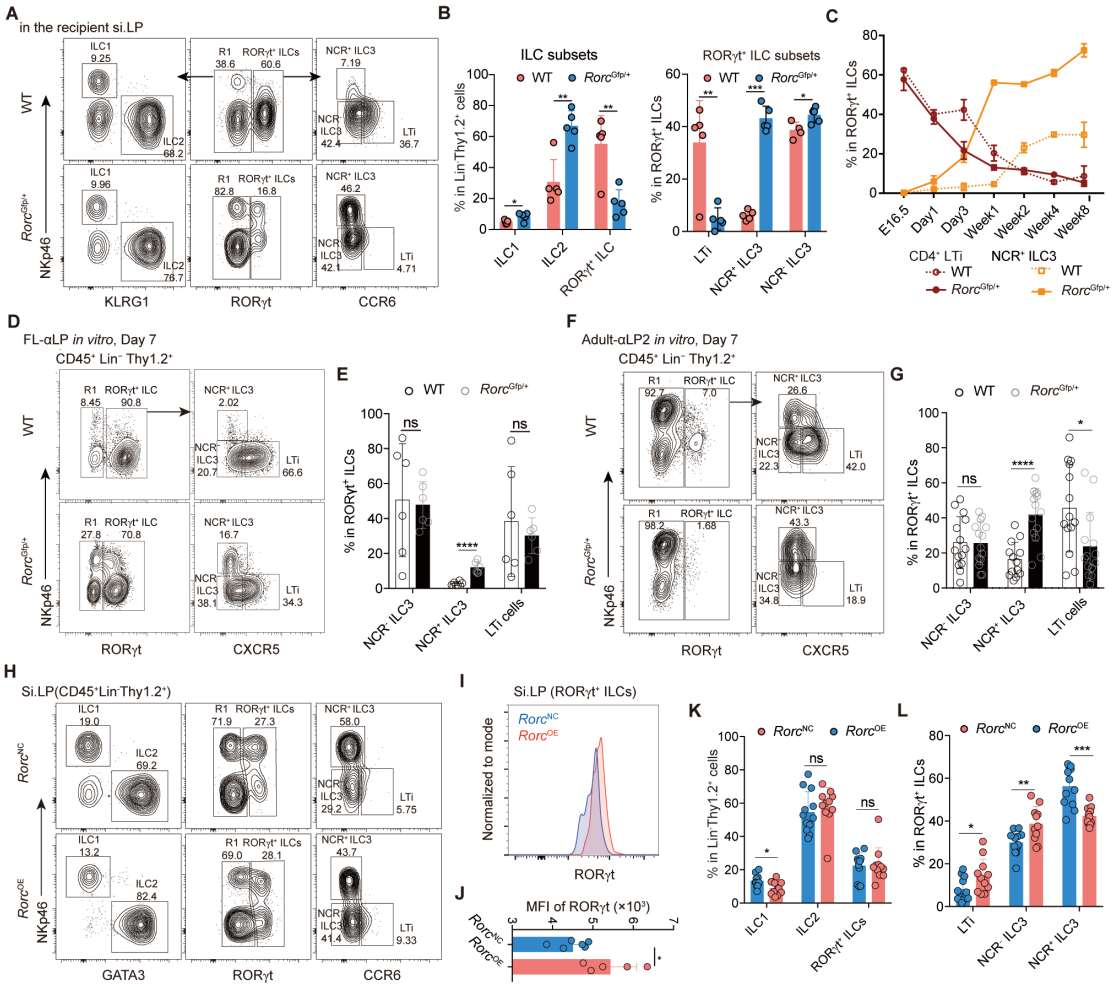

Figure S11 RORγt reduction promotes NCR⁺ ILC3 differentiation. Related to Figure 5.

(A) Representative FACS plots show the small intestinal ILC subsets derived from wide type (WT) and *Rorc*$^{Gfp/+}$ bone marrow progenitor (Lin^{-}c-Kit^{+} cells) and in the recipient mice.

(B) The percentage of major ILC subsets in (A). Data (n=5-6 per group) are pooled from two independent experiments and shown as mean ± SD.

(C) Percentage of NCR^{+} ILC3 and CD4^{+} LTi cells in the small intestine of both wide type and *Rorc*$^{Gfp/+}$ mice during ontogeny.

(D-G) Fetal liver αLPs or adult bone marrow αLP2s are sorted from wide type and *Rorc*$^{Gfp/+}$ mice for *in vitro* culture supplemented with IL-7 and SCF for 7 days. FACS plots and percentage of RORγt^{+} ILC subsets among the (D and E) fetal liver-derived and (F-G) adult bone marrow-derived daughter cells were shown. Each circle in the graph represented a biological replicate (n=6-14 per group pooled from two to five independent experiments).

(H-L) LSK from adult *Rorc*$^{Gfp/+}$ mice were transduced by empty (*Rorc*^{NC}) or *Rorc* (*Rorc*^{OE}) plasmid. (H) Flow cytometry showing the small intestinal ILC subsets in the recipient mice. (I) Intracellular RORγt staining and (J) indicated MFI in intestinal RORγt^{+} ILCs in (H). (K-L) Percentage of major ILC subsets derived from empty (*Rorc*^{NC}) or *Rorc* (*Rorc*^{OE}) plasmid-transduced progenitors. Data (n=8-9 per group) are pooled from three independent experiments and shown as mean ± SD.